Green Chemical Technology

SCIEPublish

Article

Selective Interfacial Separation of Lithium-Ion Battery Cathodes by a Chelator-Engineered Deep Eutectic Solvent: Foil Liberation, Black-Mass Purity, and Process Windows

Paul Afreh *, Zhiqin Qin, Lizhen Gao * and Muhammad Tariq

School of Chemistry and Chemical Engineering, Shanxi University (Wucheng Campus), No. 92, Wucheng Road, Xiaodian District, Taiyuan 030006, China; qinzhiqin1@sxu.edu.cn (Z.Q.); tariqmuhammad@sxu.edu.cn (M.T.)

* Corresponding author. E-mail: afrehpaul@sxu.edu.cn (P.A.); gaolizhen@sxu.edu.cn (L.G.)

Received: 27 April 2026; Revised: 23 June 2026; Accepted: 29 June 2026; Available online: 28 July 2026

ABSTRACT: Direct recycling of spent lithium-ion batteries requires selective dissociation of the cathode coating on the aluminum current collectors while minimizing cross-contamination of the recovered fractions. In this study, a chelator-based deep eutectic solvent (ChelaDES) made of levulinyl hydroxamic acid, glyceric acid, and trimethyl (2-methoxyethyl) ammonium chloride was designed as a low-temperature solvent for the selective interfacial separation of LCO, LFP, and NCA cathodes. The method uses four complementary key performance indicators (KPIs) as interfacial separation performance measures: active material removal, mass removed per unit area, bare-Al exposure, and delamination severity score. LCO showed the fastest response, reaching 93.7% active-material removal and >99% bare-Al exposure at 90 °C for 60 min. NCA showed intermediate behavior, reaching approximately 92.5% removal and 82% bare-Al exposure, while LFP exhibited threshold-controlled delamination, reaching 90.8% removal but only 66% bare-Al exposure under the same conditions. Among the kinetic models tested, the PSO-Arrhenius model provided the best overall fit for process comparison, giving apparent activation energies of 25.5, 26.5, and 28.5 kJ·mol^{-1} for LCO, NCA, and LFP, respectively. A strong correlation was observed for all chemistries between the removed mass per area and bare-Al exposure, which proves to be a useful, rapid quantitative proxy of foil liberation. Further purification studies with SEM-EDXS, XPS, and TGA/DTG suggested that the recovered black mass contained minimal impurities with minimal Al/Cu carryover (<0.1 wt%) and that the aluminum foil remained largely intact. Process heatmaps define the chemistry-specific operating windows, demonstrating that selective interfacial weakening, not bulk dissolution, controls separation. The process, therefore, acts as an upstream selective delamination and purification step, producing cleaner recovered black mass while preserving the current collector.

Keywords: ChelaDES; Lithium-ion battery; Delamination; LCO; LFP; NCA; Fickian diffusion model; Avrami model; Sustainable recycling; Binder–metal coordination; Thermal delamination

1. Introduction

The rapid rate of lithium-ion battery (LIB) growth has led to an increasing demand to establish efficient, low-energy, and chemically selective recycling techniques. The main challenges in direct recycling are not only the elimination of the cathode coating but also the design of a selective separation pathway that separates the active layer from the aluminum current collector while maintaining the integrity and purity of both recovered fractions. Traditional recycling methods such as pyrometallurgy, hydrometallurgy, and solvent leaching are normally attributed to severe shortcomings [1–4]. They are normally energy-consuming operations, produce harmful waste, and corrode aluminum foil, thus reducing the purity of the material recovered [5,6]. Conventional thermal or mechanical delamination techniques might be effective in some contexts, but they can degrade polymer binders, add impurities, or absorb large quantities of energy. Therefore, they are not very scalable or friendly to the environment. Direct recycling methods are beneficial because upstream separation methods do not modify the crystal structure or morphology of the cathode materials and enable the recovery of intact current collectors [7]. A more convenient process for direct recycling is hence foil liberation under controlled interfacial disruption as opposed to coating removal *per se*.

Deep eutectic solvents (DESs) have become promising alternatives. Compared with conventional mineral-acid hydrometallurgical processes, DESs allow adjustable acidity, which provides more control over the coordination environment and transport properties of the solvents. Deep eutectic solvents (DESs) have emerged as alternatives to traditional recycling methods. They can be tailored to binder-cathode interfaces via acidity, a hydrogen bonding environment, and coordination chemistry without the use of very corrosive mineral acids. Compared with traditional mineral-acid hydrometallurgical procedures, DESs permit variable acidity, offering greater control over the coordination environment and transport properties of the solvents [8]. Most DES formulations, however, do not have a particular affinity for the metal oxides commonly employed in cathode coatings, and their effectiveness in cathode delamination is therefore restricted [9,10]. Additionally, despite being more environmentally friendly due to low volatility, high solvation capacity, and adaptable hydrogen-bond networks [5,7], direct recycling has not yet been thoroughly developed with the use of DESs. In addition, none of the existing DESs have been deployed in the delamination process of common cathode chemistries of LCO, LFP, and NCA in a manner that fully conserves the aluminum foil. Thus, impurities in the recovered active material can be minimized, and the chemical hazard and energy consumption can be reduced. In addition, past applications of DESs have mostly been limited to leaching or binary systems, with little control over interfacial phenomena.

This study synthesizes a new form of chelator-based ternary DES (ChelaDES), which involves bioderived levulinyl hydroxamic acid (LH) as a targeted metal-coordination agent, quaternary ammonium (glyceric acid, GA), and polyol compounds (trimethyl (2-methoxyethyl) ammonium chloride). This system uses hydroxamic acid as a strong ligand in the coordination of metals, especially at the binder metal interfaces of LCO, LFP, and NCA cathodes. Hydroxamic acids are also extensively reported as strong ligands in the coordination of metals, and in addition, the IR shifts in the carbonyl/N-O regions are generally employed as markers of hydrogen bonding and complexation conditions [11]. Specifically, levulinic acid and levulinic acid-derived leachants, such as Li, Ni, Co, and Mn, are currently being developed as more sustainable reagents for the recovery of important metals from LIB black masses. This formulation can enhance solvation and permit thermal control of the delamination of large LIB cathode chemistries. ChelaDES makes use of hydroxamate-mediated metal coordination to soften the binder, which may provide a green and closed-loop process that enables direct cathode recycling. The purpose of developing this novel formulation is to develop a microenvironment that selectively disrupts binder cohesion and coating-foil interfacial adhesion but does not disrupt thermal degradation. The polymer binder is therefore free to release in its original form, facilitating easy separation of the active material, and the aluminum foil facilitates reduced impurity recycling.

The bonding between the cathode and the binder, especially in cathodes made of PVDF-based composites, is one of the greatest issues in recycling processes. These cathodes are not resistant to mild aqueous treatment and frequently need harsh solvents, high temperatures, or vigorous processing to strip the coating layers [5,6]. Conventional procedures are usually based on the use of hazardous chemicals or aqueous solutions, which can lead to corrosion and undesirable side reactions. ChelaDES, on the other hand, provides a low-energy alternative that is environmentally friendly yet consumes less toxic solvents and delaminates a broad range of cathode materials with high efficiency.

In addition, the primary limitation of any current technique of delamination is that there are no standard, quantitative measurements to directly compare delamination accuracy with the purity of the black mass and downstream process performance [9]. To address this, we integrated the ChelaDES delamination procedure with a quantitative assessment scheme, which quantifies significant amounts, such as the degree of aluminum exposure, mode of detachment, residue morphology, and mass-corrected removal fraction. Metrics provide a universal way to assess the effectiveness of the delamination process and its impact on material recovery.

To provide a mechanistic description of the delamination transformation, we applied the Avrami kinetic model and the Fickian diffusion model, which provides a quantitative analysis of delamination nucleation and growth behavior in various cathode chemistries. The model provides insight into the kinetic mechanisms that govern the release of the coating and can be used to improve the degree of delamination of a specific cathode material. This paper uses a combination of chemical rationality, kinetic modeling, and standardized assessment to offer a mechanistically based approach to electrode delamination that enables a scalable and sustainable approach to LIB recycling.

This study highlights the fact that ChelaDES can be a versatile and efficient technology for recycling direct cathodes that can operate with low-energy input and minimize the number of impurities in the produced material. ChelaDES has also demonstrated that it can obtain impurity-free materials with a wide range of cathode materials through systemic thermal reactions at temperatures ranging from 40–90 °C for 15–60 min, and it may serve as a sustainable foundation of LIB circularity.

The technical question that is answered by the study's dataset is not whether the coating is removed but how the removal process changes kinetically with the cathode chemistries (LCO, LFP and NCA) and chemistry-specific operating windows and the mechanistic conclusions that are drawn regarding the relationships among (i) foil liberation, (ii) exposure of the bare-Al and (iii) model-derived rate constants and temperature sensitivity indicators.

2. Methodology

2.1. Materials and Reagents

Spent LIBs were used as cathode materials. High-energy density and oxide-based LCOs were purchased from Taiyuan, and phosphate-based LFP (stable) and NCA (Ni-rich and high-capacity) were donated by Shanxi Yaxin Newenergy Technology (Taiyuan, China). Levulinic acid, hydroxylamine hydrochloride, choline chloride, iodomethane hydrochloride, glycerol, 2,2,6,6-tetramethylpiperidine-1-oxyl (TEMPO), NaClO, and NaBr with purities of >98% were purchased from Shanghai Hul Metechnology Co., Ltd. (Shanghai, China). Ethanol, acetone, and ethyl acetate were used as anhydrous solvents. Amberlite IRA-400 resin was used for anion exchange.

2.2. Preparation and Characterization of the Selective Separation Medium

The levulinyl hydroxamic acid (Figure 1), glyceric acid (Figure S2), and trimethyl (2-methoxyethyl) ammonium chloride were mixed in a 2:1:1 molar ratio to produce a homogenous and stable liquid phase that had both the hydrogen-bonding and coordination capabilities. The CH_3 signal trimethyl (2-

methoxyethyl) ammonium chloride was detected by ^{1}H NMR (Bruker 400 MHz, CDCl3) at 3.2 ppm (9H, s), and the O-CH_2 signal was detected at 3.6 ppm (Figure S1). The stability of ChelaDES was confirmed by the lack of phase separation after 7 days at room temperature (Figure S3). The FTIR characterization ensured that the hydroxamate- and carboxylate-bearing functionalities responsible for the interfacial separation were retained whilst the strategy of the formulation was chosen to ensure maximum interaction of binder and selective weakening of the coating-foil interface (see supplementary for details).

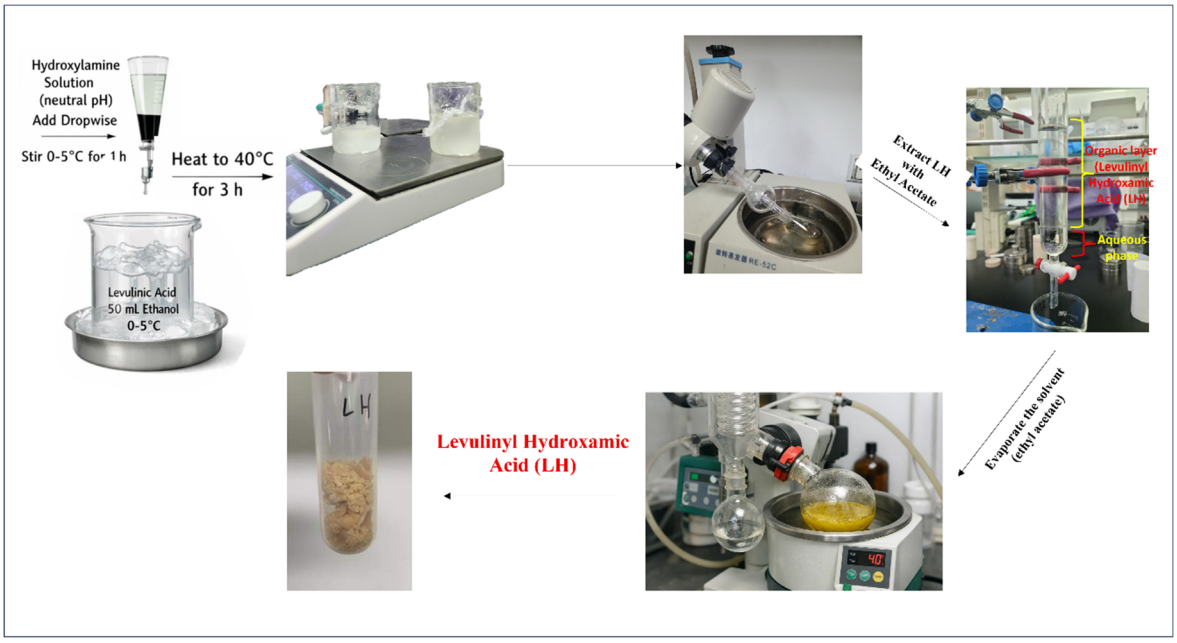

Figure 1. Schematic representation of the synthesis of levulinyl hydroxamic acid (LH), showing the low-temperature hydroxylamine addition, controlled heating, liquid-liquid extraction, and solvent evaporation sequences used to obtain the isolated product of LH.

2.3. Cathode Preparation, Selective Delamination, and Black-Mass Recovery

Fixed geometry cathode coupons (2 × 3 cm with a double-sided coating) were pre-treated with 10 mL of ChelaDES at a solid to liquid ratio of 1:50 (*w*/*v*). This was treated at a controlled temperature of 40–90 °C and an agitation rate of 300 rpm under a 15–60 min reaction period (Figure S4). The coupons were rinsed, dried, and reweighed after treatment in a bid to ascertain interfacial separation performance. The solids that had been liberated on the foil and vessel were vacuum-filtered and washed with ethanol to get rid of the remaining solvent, dried to a constant mass, and size-conditioned by milling and sieving. This process is defined in a systematic purification sequence, with the initial stage being selective interfacial weakening, followed by the removal of solvent residue aided by the wash to get a recovery-ready black mass. The weight of the active material removed was determined via blank-corrected values as follows Equation (1):

$$\text{Active removed(mg)} = (m_0 - m_1) - \Delta m_{\text{blank}} \quad (1)$$

This combined workflow guaranteed uniform preparation of the sample, controlled thermal exposure, and accurate measurement of the delamination performance of all the cathode chemistries.

2.4. Separation-Performance Metrics and Purification Metrics

Four complementary indicators that included removal fraction, mass removed per unit area, bare-Al exposure, and delamination severity score were used to measure process performance. Among these, bare-Al exposure was found to be the most practically relevant endpoint since it measures foil liberation itself,

as compared to removed mass per unit area, which measures the degree of coating release and gives a scale-relevant engineering measure. The percentage of bare Al was measured via the Otsu thresholding algorithm via ImageJ (NIH) software (version 1.54) to divide the coated and exposed areas of aluminum, which were averaged on both sides (Figure S5). The categorization of residues (0–2 scale) revealed low levels of contamination in the runs, which favor cleaner recovery [12,13]. The main endpoints were the percentage of bare Al exposure (through ImageJ analysis) and mass-based removal, which were corrected with the help of blank Al controls to remove the adsorption of the solvent [14]. Delamination scoring rubric (Table 1) helps transform visual interfacial separation into an operational severity index that can aid the selection of the process and scale-up.

The removal fraction (R) was calculated as follows Equation (2):

$$R = \frac{m_0^{\text{coated}} - m_1^{\text{post}}}{m_0^{\text{coated}} - m_0^{\text{Al}}} \quad (2)$$

where m_0^{coated} is the initial coated electrode mass, m_1^{post} is the post-delamination mass, and m_0^{Al} is the reference aluminum current-collector mass. The derived metrics included the removal percentage ($R \times 100$) and removed mass per unit area (mg·cm^{-2}).

Table 1. Delamination scoring rubric that outlines the bare Al exposure range (0–5) and a description of the operation of coating detachment.

Score	% Bare Al (15 min to 60 min)	Operational Description
0	0–1%	No visible lifting; coating intact
1	>1–10%	Edge swelling/lifting; minor detachment
2	>10–30%	Partial detachment; majority adhered
3	>30–70%	Substantial detachment; mixed adhered regions
4	>70–95%	Near complete detachment; small islands remaining
5	>95%	Complete detachment; Al largely exposed

2.5. Interfacial and Purification Characterization

XPS, SEM, EDXS, and TGA/DTG were used to analyze the interfacial and product quality. Posttreatment surface exposure of Al and depletion of the signals of the binder and oxide related to XPS were monitored. The morphology changes caused by the release of the coating and interfacial failure were resolved via SEM, and EDXS was employed to confirm the purity of the elements contained in the recovered black mass and the carryover of the Al/Cu. The TGA/DTG ratio was employed as an independent variable for the residual coating content during separation. These measurements are to be characterized in the reframe as all-purpose purification diagnostics and not just as mechanistic instrumentation.

2.6. Process Modeling and Statistics

Process behavior was determined by means of kinetic and transport analysis, but was not defined. Four kinetic models were applied to describe the delamination progress. Fickian-diffusion description of transport-limited interfacial separation as well as the Arrhenius-derived thermal barriers for process–window comparison across chemistries. The PSO/PFO, Avrami, and Q_{10} analyses are used to support the process narrative, not to control it. The experiments were conducted in triplicate (n = 3) (Table S1), randomized, and blindly scored. R (v4.3.1) was used to process the data. Pearson correlations were used to evaluate the relationships between measures (Table S2). The visualization was performed in heatmaps in OriginPro 2026.

The pseudo-first-order (PFO) model assumes a rate proportional to the remaining intact interface (3):

$$\frac{dR}{dt} = k_1(1-R) \Rightarrow \ln(1-R) = -k_1 t \tag{3}$$

where k_1 (min^{-1}) is the first-order rate constant. The pseudo-second-order (PSO) model assumes a bimolecular detachment mechanism (4):

$$\frac{dR}{dt} = k_2(1-R)^2 \Rightarrow \frac{R}{1-R} = k_2 t \tag{4}$$

where k_2 (min^{-1}) is the second-order rate constant. Linear regression of $\ln(1-R)$ versus t (PFO) and $R/(1-R)$ versus t (PSO) provided rate constants and coefficients of determination (R^2). The temperature dependence was analyzed via Arrhenius plots ($\ln k$ versus $1/T$) to extract apparent activation energies (E_a). The thermal sensitivity coefficient Q_{10} was calculated as (5):

$$Q_{10} = exp\left[\frac{E_a}{R}\left(\frac{1}{T} - \frac{1}{T+10}\right)\right] \tag{5}$$

To model the kinetics of delamination, the Avrami equation was linearized into its logarithmic form (6).

$$\theta(t) = 1 - exp^{(-ktn)} \tag{6}$$

where $\theta(t)$ is the fraction of the material that has undergone transformation at time t, k is a temperature-dependent rate constant incorporating nucleation and growth rates, and n is the Avrami exponent, a dimensionless parameter reflecting the nucleation mechanism (site-saturated or continuous) and growth dimensionality (typically 1–4; n = 4 for 3D growth with continuous nucleation). Plots of ln[−ln(1 − α)] versus ln t were constructed for each chemistry, yielding fits with Avrami exponents n decreasing from 0.9–4.3 at lower temperatures (40–60 °C) to 0.3–0.9 at higher temperatures (70–90 °C), and rate constants k increasing with temperature. This indicates a shift from nucleation-dominated (higher n) to diffusion-limited (lower n) mechanisms, with good linearity (R^2 0.85–0.98), supporting transport-controlled interfacial softening across LCO (n = 0.25–0.87), LFP (n = 0.39–4.34), and NCA (n = 0.34–2.42).

The Fickian diffusion model is based on the analytical solution for diffusion into a slab with constant surface concentration (instantaneous saturation at the coating surface due to agitation and solvent excess) (7):

$$f(t) = 1 - \sum_{n=0}^{\infty} \frac{8}{(2n+1)^2\pi^2} \exp\left(-\frac{(2n+1)^2\pi^2\alpha t}{4}\right) \tag{7}$$

where $\alpha = D/L^2$ is the effective diffusivity parameter (in min^{-1}), D is the effective diffusion coefficient of ChelaDES components through the coating, and L is the effective half-thickness of the coating layer. The series is truncated at $n = 19$ for computational accuracy (convergence is rapid for practical α values).

The temperature dependence of α follows the Arrhenius Equation (8):

$$\alpha(T) = A \exp\left(-\frac{E_a}{RT}\right) \tag{8}$$

where T is the temperature in Kelvin, $R = 8.314$ J/mol·K is the gas constant, E_a is the activation energy (in kJ/mol), and A is the pre-exponential factor (in min^{-1}).

3. Results and Discussion

3.1. Physicochemical Confirmation of ChelaDES Formation

ChelaDES contains the functional groups required to selectively separate interfaces such as hydroxamate-associated C=O and N–H bands of LH in the range of 3200–3500 cm^{-1}, broad O–H/N–H absorption, and carboxyl-derived O–H/C=O bands at 1700 cm^{-1} of GA. The shifts in C=O and N–O and the significant broadening of the O–H/N–H envelope are evidence of the appearance of an extended and hydrogen-bonded and ionically associated network in the ternary liquid. The spectral characteristics

indicate that ChelaDES is endowed with good solvation capacity and coordinated active oxygen donor sites, which enable it to enter the binder-rich coating domain, promote PVDF swelling, and selectively weaken the coating-foil interface without necessarily using aggressive bulk dissolution. In this regard, the FTIR spectrum is used to support the interpretation of ChelaDES as a favorable interfacial separation mediator, the functionality of which is due to the non-competitive interaction of hydrogen bonding, ionic association, and hydroxamate-based coordination (Figure 2a). Considering that hydroxamic acids are known metal chelators, usually coordinating themselves to carbonyl and hydroxamate oxygen donors with diagnostic IR shifts, the preserved and shifted LH bands confirm that ChelaDES combines both solvation and coordination properties in a single liquid phase, as opposed to acting as a pure carrier medium [11]. This ratio (C-OMe:LH:GA = 1:2:1) maximized viscosity and hydrogen bonding to coordinate metals, as indicated by the lower melting points than those of some of the components. The ternary system was more selective for LIB cathodes than binary systems, as acidic (LH), quaternary ammonium (C-OMe), and polyol (GA) functions were incorporated, thereby allowing binder swelling and metal leaching without strong acids [15,16]. FTIR analysis confirmed that the ChelaDES formulation combines hydrogen-bonding functionality with hydroxamate-bearing coordination sites, thereby creating a solvent environment suited to selective interfacial weakening rather than bulk mineral-acid dissolution. To further support the formation of the eutectic liquid, differential scanning calorimetry (DSC) was carried out for the individual components and the formulated ChelaDES. Deep eutectic solvent formation is commonly associated with a pronounced depression or suppression of the melting/freezing transitions of the parent hydrogen-bond donor and acceptor components, caused by strong hydrogen-bonding and ionic interactions within the liquid network [17–19]. As shown in Figure 2b, the individual components display distinct thermal transitions, whereas the ChelaDES formulation shows a suppressed and broadened thermal response without the separate sharp melting events of the parent compounds. This behavior is consistent with eutectic formation rather than a simple physical mixture. Together with the FTIR band shifts associated with hydrogen bonding and hydroxamate/carboxylate interactions, the DSC result supports the formation of a homogeneous ChelaDES phase suitable for interfacial cathode delamination [18–20].

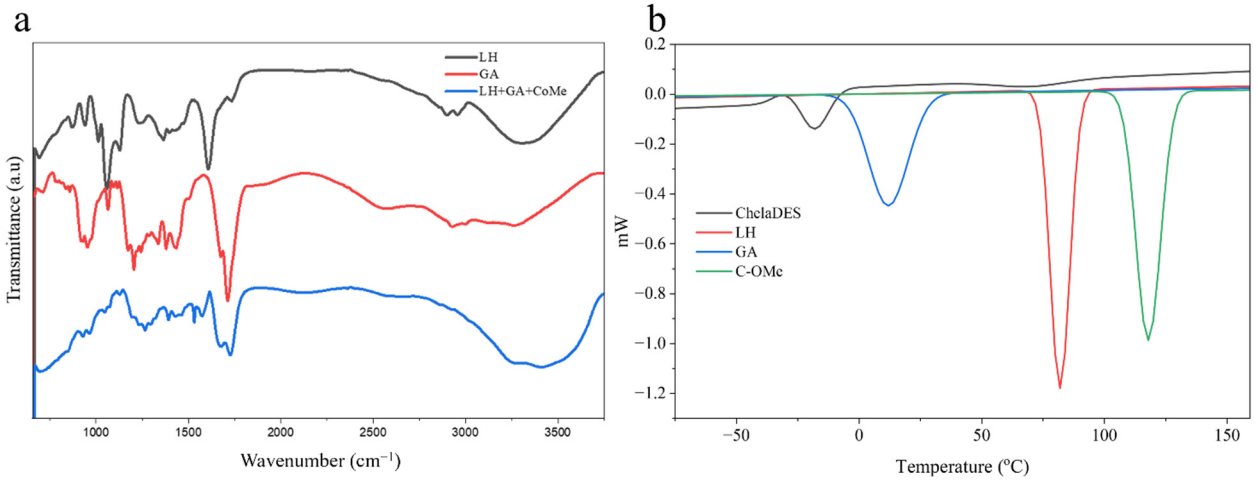

Figure 2. Physicochemical characterization of ChelaDES. (**a**) FTIR spectra showing hydrogen-bonding and coordination-related shifts in the ChelaDES formulation. (**b**) DSC thermograms of the individual components and ChelaDES, showing suppression/broadening of the parent-component melting transitions and supporting eutectic formation through melting-point depression.

3.2. Interfacial Separation Performance and Foil Liberation Across Cathode Chemistries

The effectiveness of ChelaDES-mediated selective separation is measured with four complementary key performance indicators (KPIs) that are combined to describe the liberation of cathode active materials

from aluminum current collectors. These indicators/metrics, such as liberation efficiency, areal removal, bare-aluminum exposure, and delamination score, are multidimensional assessments that measure the extent and quality of the separation process. These KPIs are not independent variables, as the systematic temperature-time mapping of the 40–90 °C operating range (Figures 3–5) reveals that the near-perfect correlations (R^2 = 0.998–1.000) between them are good proof of the measurement methodology.

The liberation efficiency (expressed as the fraction of mass removed R) is used to measure the mass-based separation performance, as illustrated by Equation (2). This metric directly addresses the main process goal, which is the recovery of cathode active materials as a separable fraction. Among the three cathode chemistries studied, the liberation efficiency is positively correlated with temperature and processing time, which is indicative of the thermally activated character of the interfacial separation process. The thermally delaminated dynamics of LCO reveal that active material removal increases monotonically with time at all temperatures [21,22]. The most pronounced temperature discrimination is observed at early reaction times and decreases as the curves move toward a late time plateau. The removal kinetics show that removal starts at the low to mid-50% range at 15 min and accelerates to approximately 80–90% range at 60 min at the study temperatures (40–90 °C). Delamination at 40 °C always lags behind higher temperatures at 30–40 min before converging at 50–60 min. Mechanistically, this "early acceleration followed by convergence" behavior is assumed to be consistent with an initial diffusion- or penetration-limited interfacial weakening step, which switches to a saturation regime once the removable fraction is largely depleted within the cathode architecture (Figure 3a) [23]. The LFP exhibited threshold-dominated delamination behavior (Figure 3b). The removal rate is low (<5%), as shown in Figure 3b, below 60 °C/40 min (Figure S4b), which is in line with the uninterrupted interfacial disruption of the retained Fe 2p, P 2p, and F 1 s features (Figure S7b). At temperatures above this threshold temperature for practical separation, however, LFP suddenly switches to a high removal regime (Figure S4b) to a high level of approximately 91% removal at 60 °C/60 min. This increased onset coincides with its increased apparent activation energy (E_a = 28.5 kJ·mol^{-1}, Figure 3c). This may suggest that an increase in energy disrupts the stability of the phosphate framework and increases binder-particle cohesion [24]. The transitional behavior of NCA shows liberation efficiencies between 53.1% and 92.5% (Figure 3c). Above temperatures of approximately 60 °C, the removal efficiency and bare Al exposure increased exponentially to 92% after 60 min. This observed temperature-dependent acceleration may be reflected in the strong correlation coefficients between the removal fraction and bare Al exposure (Figure 4b).

The separation process is further explained by the removal of mass per unit area, which is important. Areal removal (mg/cm^2) is a geometry-normalized measure that can be used to reduce sample-to-sample variability due to electrode coating thickness and active material loading. The KPI is specifically useful in the process of scale-up calculations because it allows the direct translation of laboratory performance to industrial throughput forecasting. The highest areal removal values obtained under optimized conditions are in the order LCO (59.4 mg/cm^2) > NCA (49.0 mg/cm^2) > LFP (39.0 mg/cm^2), which is a product of the active material loading and interface adhesion strength of each cathode (Figure 4).

These variations are in line with the chemistry-sensitive variations in the pre-coating loading and interfacial strength of adhesion. More importantly, the correlation plots in Figure 4d–f indicate that the removed mass per unit area is nearly proportional to the bare-Al exposure, with R^2 values of 0.998–1.000 for all three chemistries. Such a close correspondence shows that gravimetric release and foil exposure follow each other quite closely. In terms of process control, this implies that the mass per unit area removed can serve as a strong proxy for foil liberation. On the other hand, it may have direct implications for the calculations of reactor productivity and material handling. Thus, they are interchangeable when measured to evaluate process performance assessment. The areal removal and bare-aluminum exposure are directly proportional to each other, as demonstrated through the linear correlation between these two measures (R^2 = 0.998–1.000 in all chemistries) (Figure 4d–f).

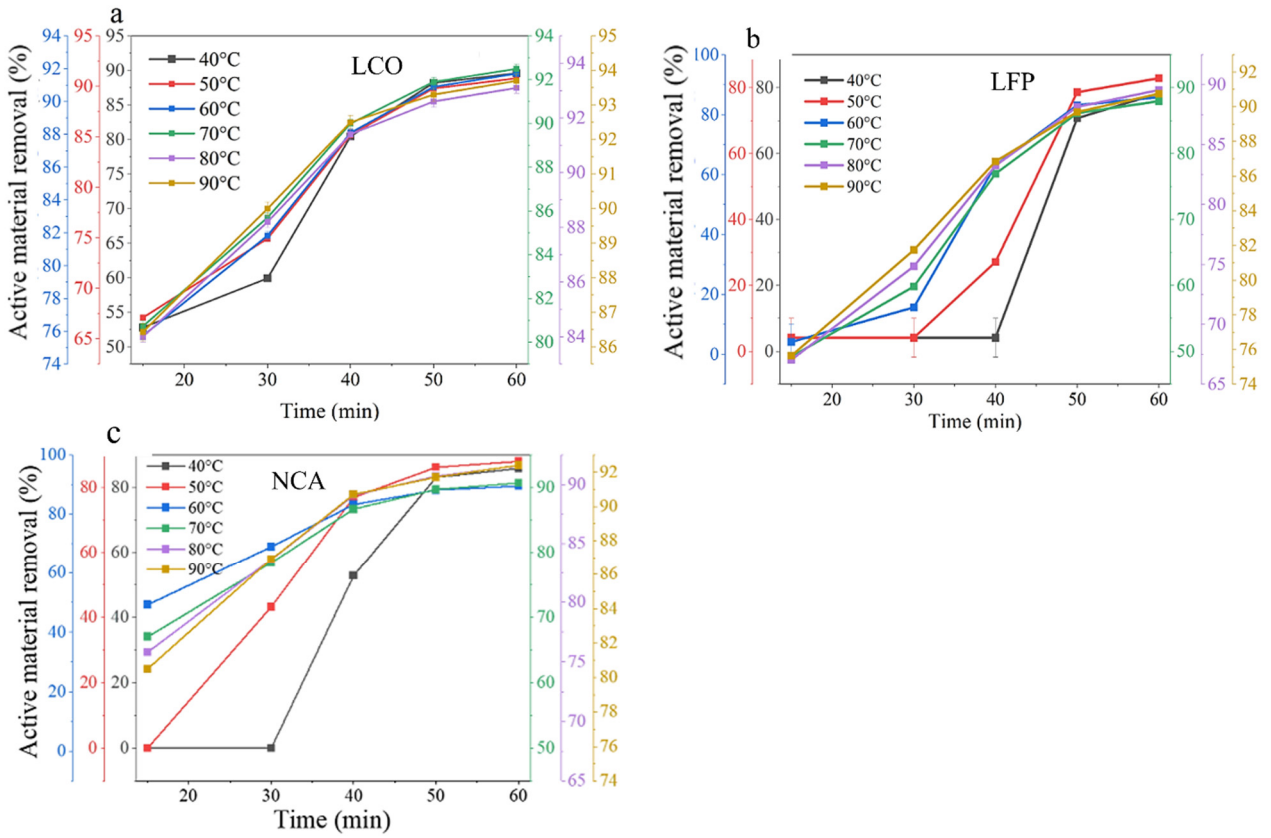

Figure 3. Thermally driven active material removal profiles of ChelaDES-treated cathodes, showing the evolution of removal efficiency with time at 40–90 °C for (**a**) LCO, (**b**) LFP, and (**c**) NCA.

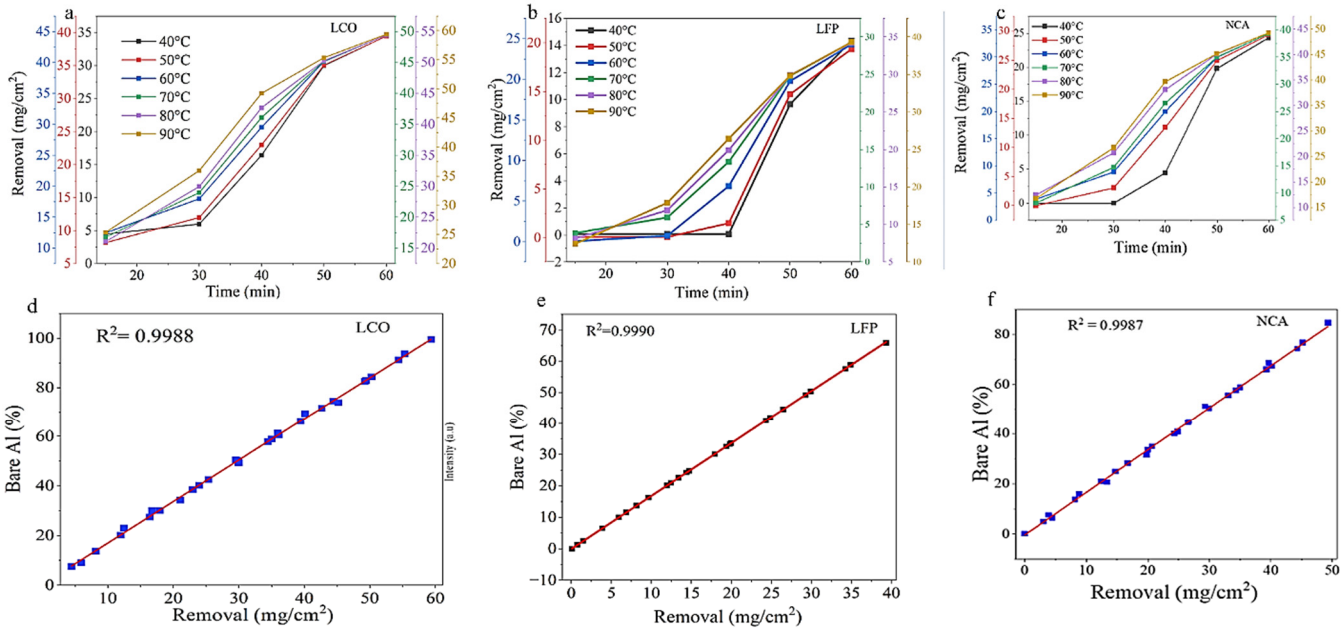

Figure 4. Temperature-dependent areal removal and its correlation with bare-Al exposure during ChelaDES delamination of different cathode chemistries: (**a**) time-resolved removal (mg·cm^{-2}) of LCO at 40–90 °C, (**b**) time-resolved removal (mg·cm^{-2}) of LFP at 40–90 °C, (**c**) time-resolved removal (mg·cm^{-2}) of NCA at 40–90 °C, (**d**) linear relationship between removal per unit area and bare-Al exposure for LCO, (**e**) linear relationship between removal per unit area and bare-Al exposure for LFP, and (**f**) linear relationship between removal per unit area and bare-Al exposure for NCA.

The most process-relevant endpoint of the four KPIs is exposure to bare aluminum, as this is the endpoint that directly quantifies the attainment of the main separation goal: foil liberation. In contrast, mass-based methods measure the total amount of material removed but do not identify productive separation and non-productive loss of material. Bare-aluminum exposure, on the other hand, measures the proportion of the current collector surface that has been exposed successfully because of selective interfacial failure. The metric is obtained via automated image processing via the Otsu thresholding algorithm on digital micrographs. This provides objective and reproducible measurements with quantifiable uncertainties. At 90 °C/60 min, LCO achieved >99% bare-Al exposure (Figure 5a), which indicated that foil liberation was almost complete. NCA reached an exposure of 82% (Figure 5c), which is quite high but not complete detachment, whereas LFP reached 66% exposure (Figure 5b), even though it achieved a high mass-based removal of 90.8%. This deviation is mechanical in nature. These tendencies are consistent with known variations in the adhesion strength of cathode chemistries, with LFP always having the highest adhesion to Al foil [23,24]. This demonstrates that LFP is capable of coating displacement under extensive conditions without fully exposing the foil, which suggests that the residual islands with binders are not fully removed from the Al surface after treatment. In practice, this implies that removal efficiency would indicate a higher quality of separation than would be the case with LFP, but bare-Al exposure would indicate a closer approximation to the actual foil recovery result.

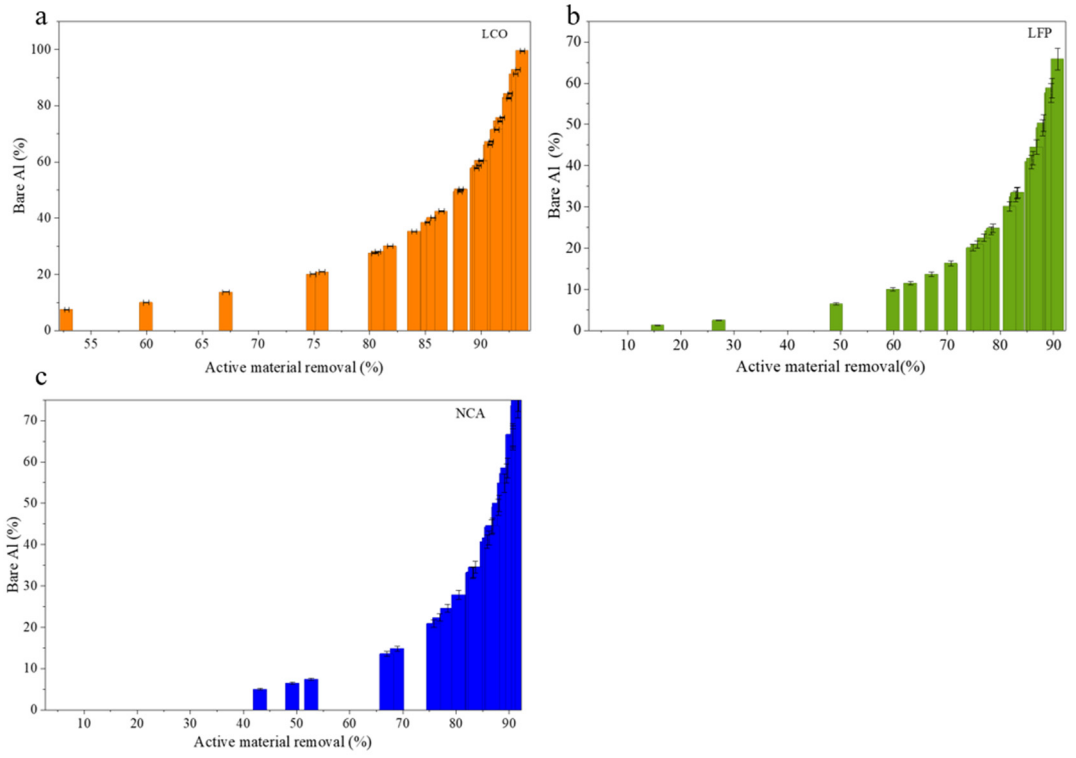

Figure 5. Bare-Al exposure as a function of active material removal for three cathode chemistries, highlighting progressive foil liberation in LCO, threshold-controlled separation in LFP, and transitional behavior in NCA: (**a**) LCO, (**b**) LFP, and (**c**) NCA.

Delamination score offers a semi-quantitative ordinal categorization (0–5 scale), which summarizes the visual representation of the interface that has been separated into a practical assessment measure that can be used in quick process monitoring and quality control tools. These foil-liberation results were used as a semi-quantitative operational measure of the delamination score. According to Table 1, a score of 0 corresponds to 0–1% bare-Al exposure, a score of 1 to >1–10%, a score of 2 to >10–30%, a score of 3 to >30–70%, a score of 4 to >70–95%, and a score of 5 to >95% exposure. This scale thus takes the gap between the foil exposure, which is obtained from images, and the real process tracking. Figure 6a–c shows

that LCOs occupy the highest severity regime in the broadest range of the operating window, with the majority of the moderate–severe conditions existing in scores of 4–5. This is consistent with nearly complete foil liberation. LFP, in contrast, was mostly in the range of 0–2 throughout a large part of the matrix, which supports the argument that detachment is minimal/partial at the onset. The terminal 66% bare-Al exposure of LFP, even under its optimum condition, falls within a score of 3, as opposed to a score of 4 or 5, which is completely in line with incomplete foil liberation. Figure 6c shows an intermediate response (NCA), which started with low-to-moderate scores under mild conditions and then shifted from milder to severe conditions at high temperatures and with increased treatment time. The final exposure of NCA was 82%, meaning that the optimized condition fell within the score range of 4. Therefore, the heatmaps in Figure 6a–c not only visualize the process response but also establish the practical operating space of each cathode chemistry and indicate that LCO is easily delaminated, NCA is state sensitive and yet manageable, and LFP is obviously threshold limited.

The interdependencies among the four KPIs are scientifically reported through correlation analysis, which reveals that the exposure of bare aluminum is the master variable. All other metrics can be predicted around it. The nearly ideal linear relationship between the bare-aluminum exposure and the mass-based liberation efficiency ($R^2 > 0.998$) of all three cathode chemistries shows that visual endpoint assessment is a valid measure of separation performance, similar to gravimetric analysis. This has major implications for process monitoring and quality assurance procedures. Moreover, the methodical difference in the KPI relationships between the three cathode chemistries, which are homogeneous, with progressive separation in LCO to threshold-limited, nonuniform separation in LFP, lays the basis for chemistry-specific process optimization, which is described in the next section.

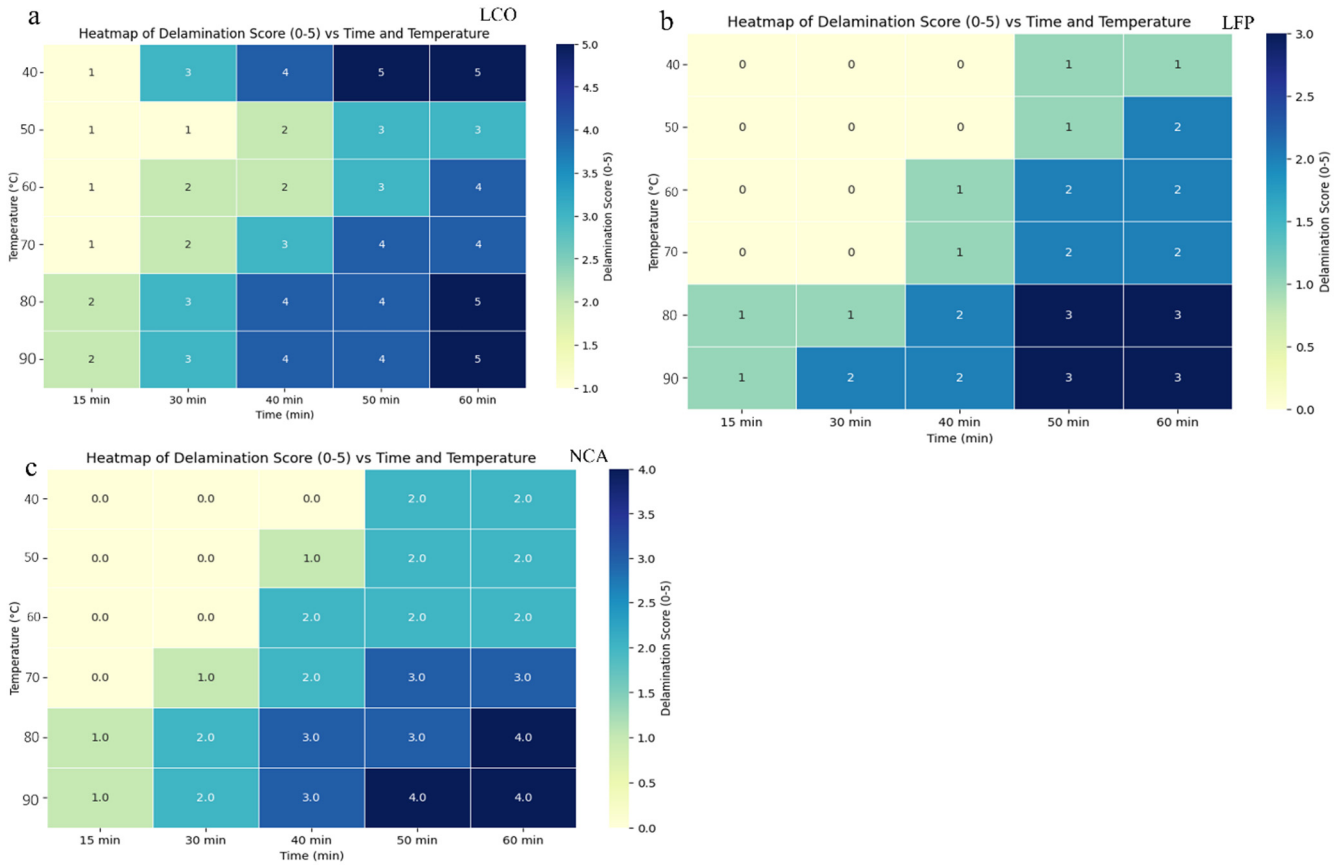

Figure 6. Temperature–time heatmaps of the delamination score (0–5) for ChelaDES-treated cathodes, illustrating the severity of interfacial separation across operating conditions for (**a**) LCO, (**b**) LFP, and (**c**) NCA.

In general, the four KPIs lead to the same mechanistic conclusion that ChelaDES favors selective interfacial failure and not a randomly disrupted coating. The overall performance of LCO was highest, with the highest level of removal of active material at 93.7% active material removal, 59.4 mg·cm^{-2} areal removal, over 99% bare-Al exposure, and a terminal delamination score of 5 under optimum conditions. NCA was followed by 92.5% removal, 49.0 mg/cm^2 area removal, 82% bare-Al contact, and a final score of 4. LFP achieved 90.8% removal and 39.0 mg/cm^2 areal removal; however, 66% bare-Al exposure and a final score of 3 verified that there was residual adhesion. These chemistry-specific variations demonstrate that no single measure can be used to evaluate the performance of ChelaDES, but a combination of KPIs, with bare-Al exposure and delamination scores, is the most informative measure of practically relevant foil liberation.

X-ray photoelectron spectroscopy (XPS) supports the argument that ChelaDES causes chemistry-dependent surface reconstruction after cathode separation, as shown by the attenuation of the coating- and binder-induced spectral features along with the simultaneous appearance of the Al substrate signal. This spectral development shows that the mechanism involves selective interfacial disruption of the coating foil interface and not random chemical attack on the current collector. Before treatment, the surface of LCO is clearly coating dominated, with significant Co 2p, C 1 s, and O 1 s contributions (Figure 7a). However, after treatment, a pronounced increase in the signal of Al 2p with a significant reduction in the signal of the cathode is observed (Figure 7d). Similar but less comprehensive changes are recorded with LFP; prior to treatment, the spectrophotometer shows high signals of Fe 2p, P 2p, C 1 s, and O 1 s, which are typical of intact phosphate-based coatings (Figure 7b). This supports the low removal rate (<5%), as shown in Figure 3a, below 60 °C/40 min (Figure S4b), which is in line with the uninterrupted interfacial disruption [25]. After separation, partial emergence of Al 2p is observed, and a significant residual intensity of the generated cathode remains, indicating partial residual adhesion between the coating and foil interface (Figure 7e). Within the scenario of NCA, the pretreatment spectrum shows strong Ni 2p, Co 2p, C 1 s, and O 1 s signals (Figure 7c), whereas the posttreatment surface gives a strong signal of Al 2p but incomplete attenuation of transition-metal signals, which is indicative of the intermediate extent of current-collector exposure (Figure 7f). These spectroscopic findings suggest that the foil liberation efficiency decreases in the following order: LCO > NCA > LFP. Thus, the effectiveness of ChelaDES is likely dictated by the cathode-chemistry-dependent interfacial selectivity.

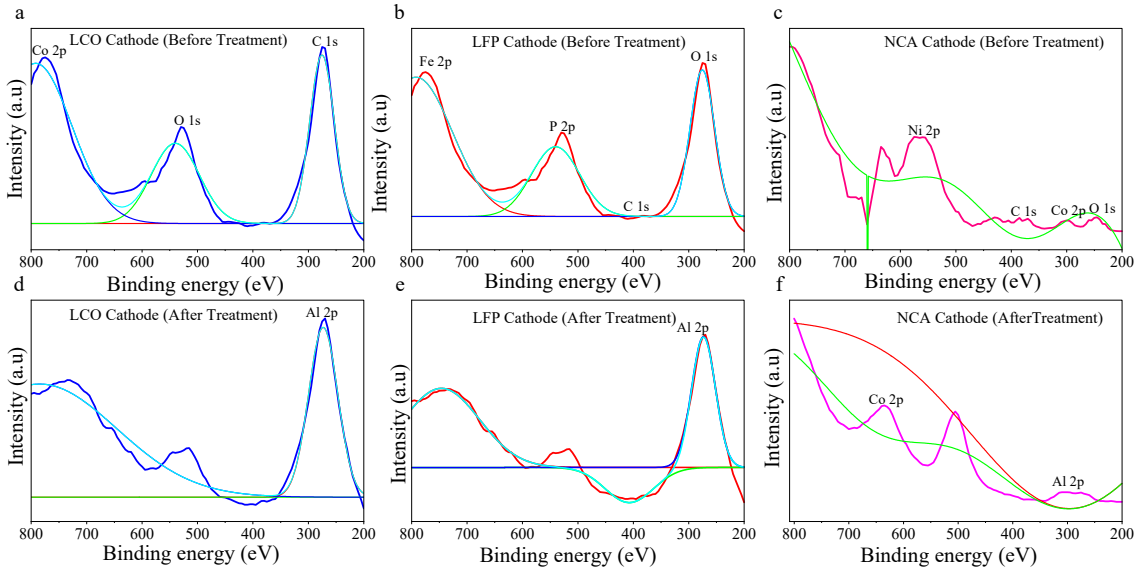

Figure 7. XPS analysis of the cathode surfaces before and after ChelaDES treatment, showing chemistry-dependent foil exposure after interfacial separation: (**a**) LCO before treatment, (**b**) LFP before treatment, (**c**) NCA before treatment, (**d**) LCO after treatment showing near-complete foil liberation, (**e**) LFP after treatment showing partial residual adhesion, and (**f**) NCA after treatment showing intermediate foil exposure.

3.3. Process Windows and Operating Envelopes for Selective Separation

The temperature-time heatmaps in Figure 8 provide a complete visualization of the separation performance space, allowing one to make rational choices regarding operating conditions for each cathode chemistry. These heatmaps convert the kinetic measurements into a process decision structure by systematizing performance measures by their place in the temperature-time array. Hence, the operating regimes that attain target separation results as well as reduced energy input. A comparative analysis of these heatmaps of the three different cathode chemistries indicates that there are three different separation regimes that constitute a decision map to apply in a mixed-stream processing situation.

3.3.1. Progressive Separation Regime (LCO)

Lithium cobalt oxide has what can be described as the desired separation behavior in process engineering principles, in that it monotonically increases with time and temperature and has no noticeable threshold effects or kinetic impediments. The liberation efficiency heatmap of LCO (Figure 8a) shows a gradual decrease in efficiency, with an efficiency of approximately 53% at 40 °C/15 min and 93.7% at 90 °C/60 min, with the gradient of the performance contour lines steepening with increasing temperature toward temperature-independent performance at higher temperatures. This saturation behavior shows that the initial interfacial adhesion strength and not the intrinsic chemical resistance limits the separation of LCO. Therefore, the process is very predictable and controllable. The corresponding heatmap of the exposure of the bare aluminum (Figure 5c) demonstrates that foil liberation occurs in a proportional manner, with scores of 4–5 (almost full exposure to complete exposure) possible in most of the studied parameter space. In practice, LCO is easily treated at moderate temperatures (60–70 °C) over long periods (45–60 min), with liberation efficiencies greater than 85% and much lower energy requirements than the optimum 90 °C/60 min.

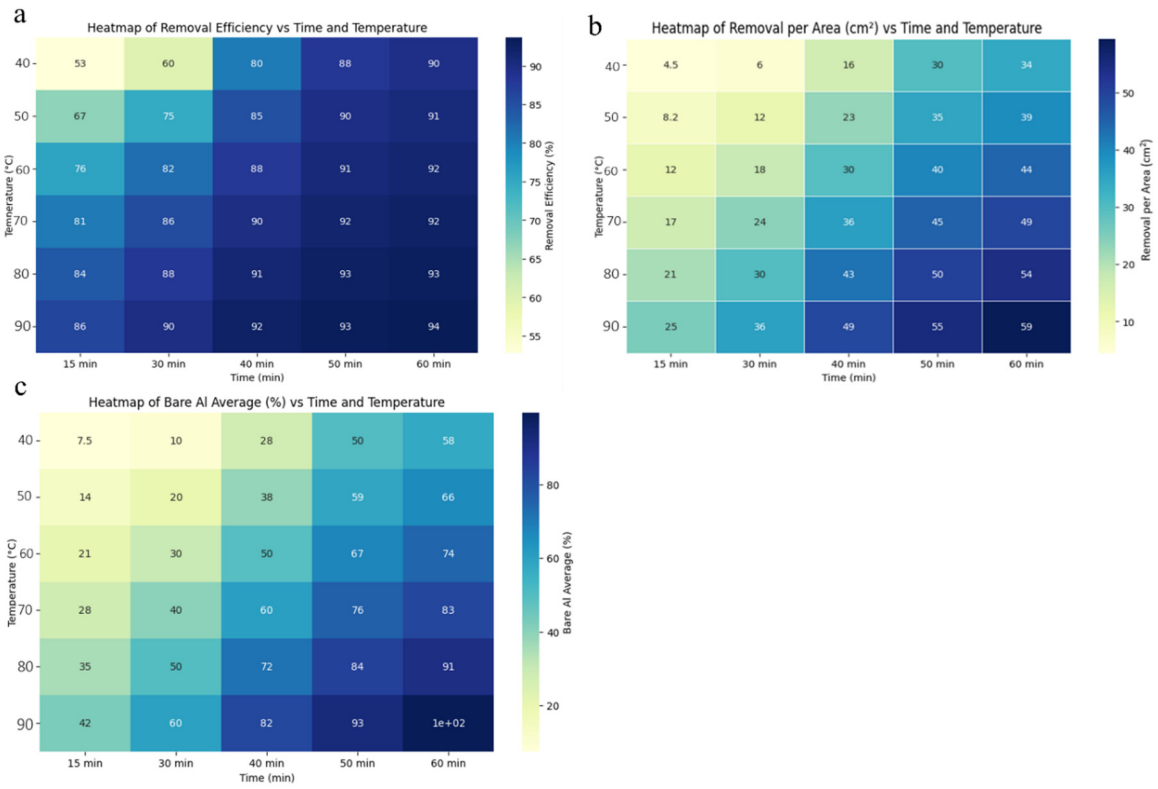

Figure 8. Temperature–time heatmaps showing the process performance of LCO during ChelaDES treatment: (**a**) active material removal efficiency (%), (**b**) removal per unit area (mg·cm^{-2}), and (**c**) bare-Al exposure (%), illustrating progressive foil liberation with increasing treatment severity.

3.3.2. Threshold-Limited Separation Regime (LFP)

Lithium iron phosphate has the most challenging separation profile, with a strong thermal threshold that must be exceeded before significant foil liberation occurs. The liberation efficiency heatmap of LFP (Figure 9a) shows an apparent discontinuity, with the efficiency being less than 10% at all temperatures below 60 °C for 40 min. Beyond this, the efficiency increases to over 80% at higher temperatures. This threshold behavior is also in line with the high structural stability of the olivine phosphate framework and the cohesion strength of the particle–binder, which has been extensively reported in the case of LFP electrodes [26]. This finding is supported by the delamination score heatmap (Figure 6b), which shows that LFP has most of its scores in the range of 0–2 (minimal to partial detachment) across the entire parameter space of interest, in contrast to LCO. The highest percentage of exposure of LFP to bare aluminum that is obtained in an optimized state (90 °C/60 min) is 66%, which is significantly less than the >95% LCO. This adhesion remnant is explained by the high thermal stability of the PVDF binders in the LFP electrode and the obstruction of the olivine structure to hydroxamate coordination. To design processes, LFP requires the entire thermal budget (at least 80% for 60 min) to achieve useful separation efficiency, and even then, complete foil liberation cannot be guaranteed.

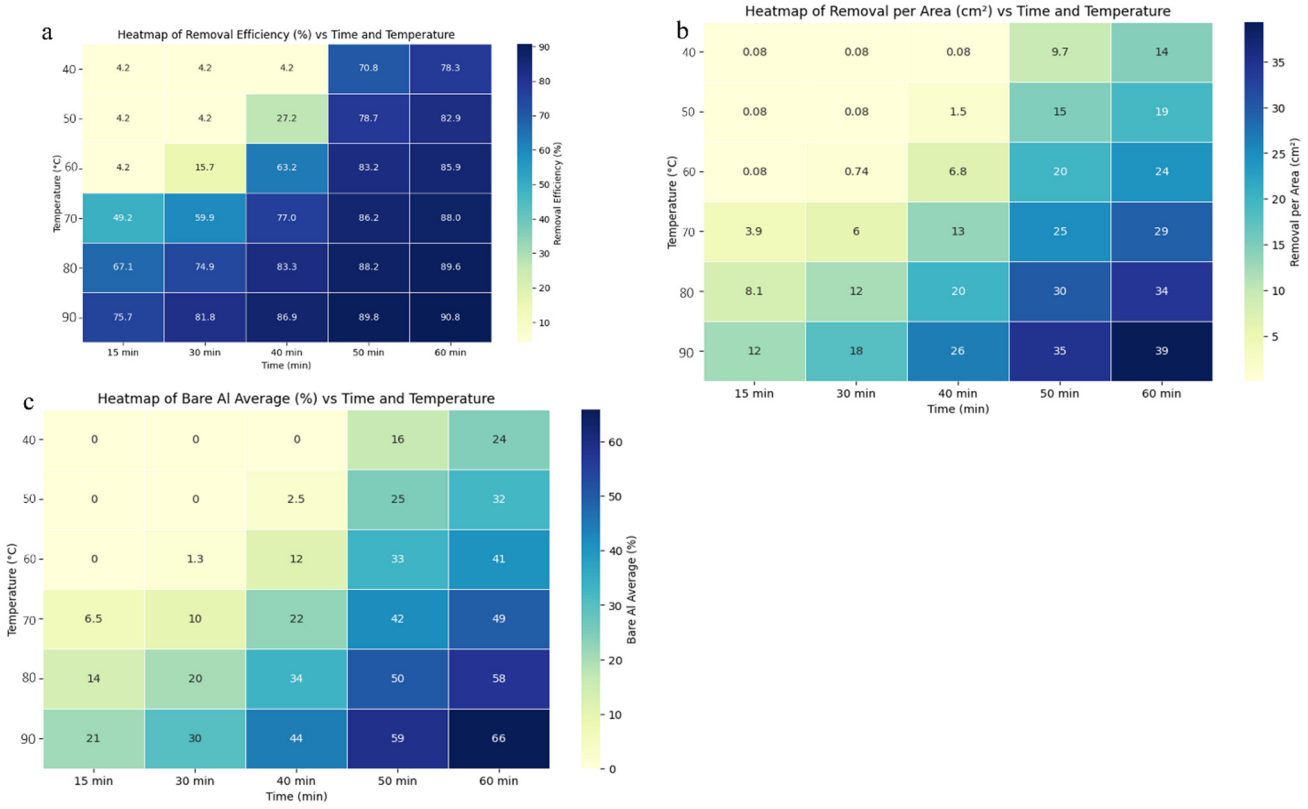

Figure 9. Temperature–time heatmaps showing the process performance of LFP during ChelaDES treatment: (**a**) active material removal efficiency (%), (**b**) removal per unit area (mg·cm^{-2}), and (**c**) bare-Al exposure (%), illustrating the threshold-controlled onset of practical foil liberation.

3.3.3. Transitional Separation Regime (NCA)

Nickel cobalt aluminum oxide occupies an intermediate state between the progressive and threshold-limited regimes, exhibiting both of these behavior patterns depending on temperature and time. The heatmap of the liberation efficiency of NCA (Figure 10a) shows a slow increase in efficiency at low temperatures, but at high temperatures, it starts accelerating at a faster rate, starting at approximately 70 °C. This mixed-metal behavior reflects the mixed metal structure of NCA (sites occupied by Ni, Co, and Al)

and the associated difference in the affinity of hydroxamate complexes for these various metal centers. This is consistent with previous results of Ni-rich cathode surface reconstruction under heat [25].

The nickel and cobalt sites are able to coordinate effectively with the hydroxamate ligands to promote interfacial softening, whereas the aluminum sites establish weaker complexes and thus might not be able to coordinate uniformly. The bare-aluminum exposure heatmap (Figure 9c) shows a transitional characteristic, as the values of the exposure are in the entire range of <10% and >80% under different conditions. To maximize the process, NCA has moderate-to-high-temperature operation (≥70 °C) to achieve efficient foil liberation without prolonged processing time at lower temperatures.

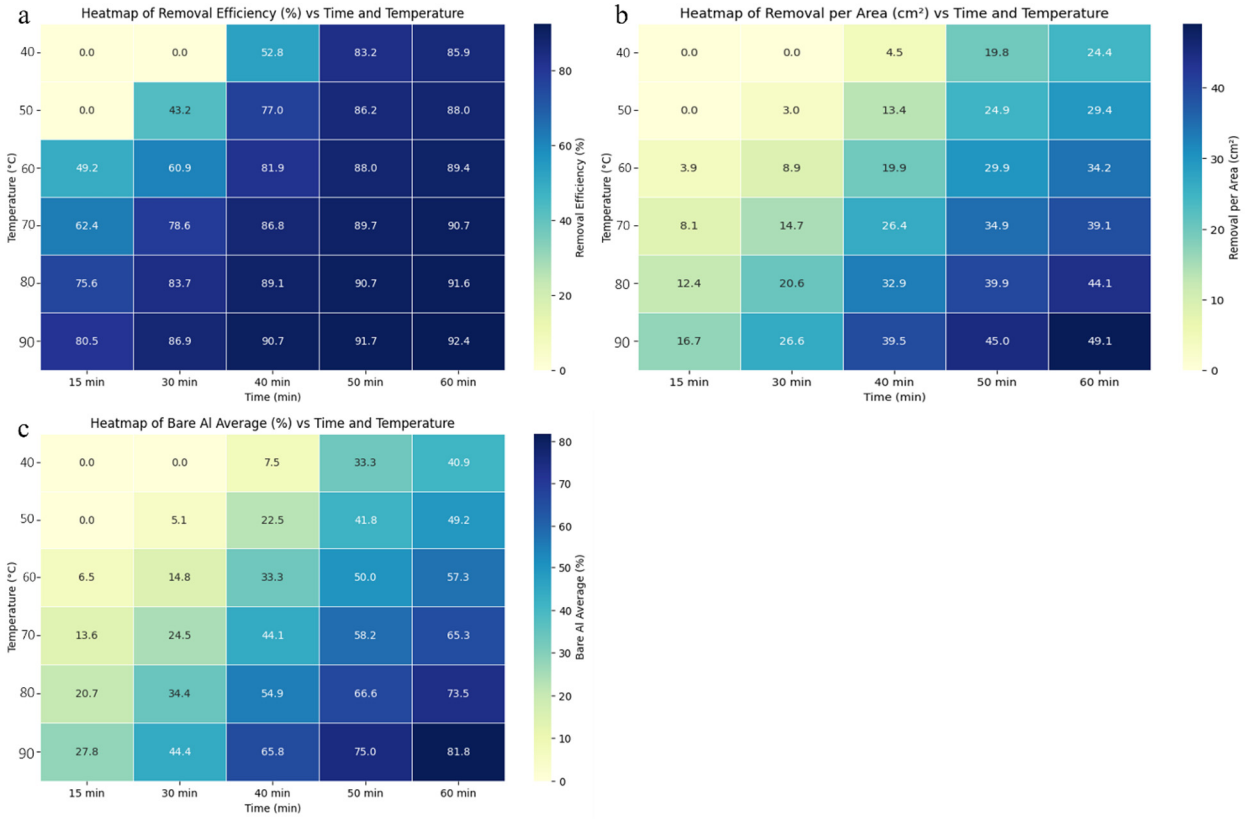

Figure 10. Temperature–time heatmaps showing the process performance of NCA during ChelaDES treatment: (**a**) active material removal efficiency (%), (**b**) removal per unit area (mg·cm^{-2}), and (**c**) bare-Al exposure (%), illustrating the transitional increase in foil liberation with increasing treatment severity.

3.3.4. Mixed-Stream Processing Decision Map

The discovery of three distinct separation regimes enables the development of a rational decision map for processing mixed cathode streams in a scenario of significant industrial importance, given that end-of-life battery feeds are heterogeneous. The decision logic proceeds as follows: (1) With feeds of mostly LCO composition, moderate temperatures of operation (60–70 °C, 45–60 min) represent an efficient trade-off between separation performance and energy consumption; (2) with feeds of mostly LFP composition, high temperatures of operation (≥80 °C, 60 min) are an absolute requirement to achieve an ideal separation efficiency, and complete foil liberation should not be expected as a baseline assumption; (3) for mixed or NCA-rich feeds, intermediate temperatures (70–80 °C, 50–60 min) represent the recommended operating point on the basis of the transitional kinetics observed. The specific activation energies (E_a = 25.5 kJ/mol for LCO, 26.5 kJ/mol for NCA, and 28.5 kJ/mol for LFP) of the chemical systems were used to quantify the relative thermal sensitivity of the systems. This gives the basic parameters used to calculate process intensification (Figure 11). The Q_{10} thermal sensitivity coefficients (1.3–1.8 experimentally *vs*. 2.0–2.4

theoretically) imply that an ideal increase in rate due to increases in temperature is moderate. At 40–90 °C, LCO has ratios of approximately 1.2–1.3, which deviates moderately from the theoretical values (Figure 11a). In contrast, LFP exhibits the greatest divergence, with ratios of 1.4–1.5. This is consistent with its high degree of particle-binder cohesion and high mechanical stability, which restricts the degree to which thermal input accelerates interfacial failure (Figure 11a). On the other hand, NCA is in the middle, with ratios of approximately 1.25–1.35, which is indicative of its threshold-like delamination behavior, as well as of the temperature-sensitive weakening of Ni-rich layered oxide surfaces [27] (Figure 11b).

Figure 11c shows the Arrhenius-derived (theoretical) Q_{10} over a wider range (20–120 °C). These chemistry-specific differences are further supported by the Arrhenius-derived values of Q_{10} derived over a wider temperature range (Figure 11c). The apparent activation energy of LCO is approximately 25.5 $kJ \cdot mol^{-1}$, and it produces a Q_{10} value of approximately 2.0, which is much closer to the theoretical value (Figure 11c). LFP has a relatively high activation energy of 28.5 $kJ \cdot mol^{-1}$. Thus, lower Q_{10} values are not experimentally active even though LFP is theoretically more sensitive. With an intermediate activation energy of 26.5 $kJ \cdot mol^{-1}$, NCA exhibits Q_{10} behavior, which begins to change abruptly at high temperatures, as expected from its thermally triggered interfacial disruption (Figure 11c). Thus, a long residence time could be more energy efficient than a temperature increase for attaining target separation performance.

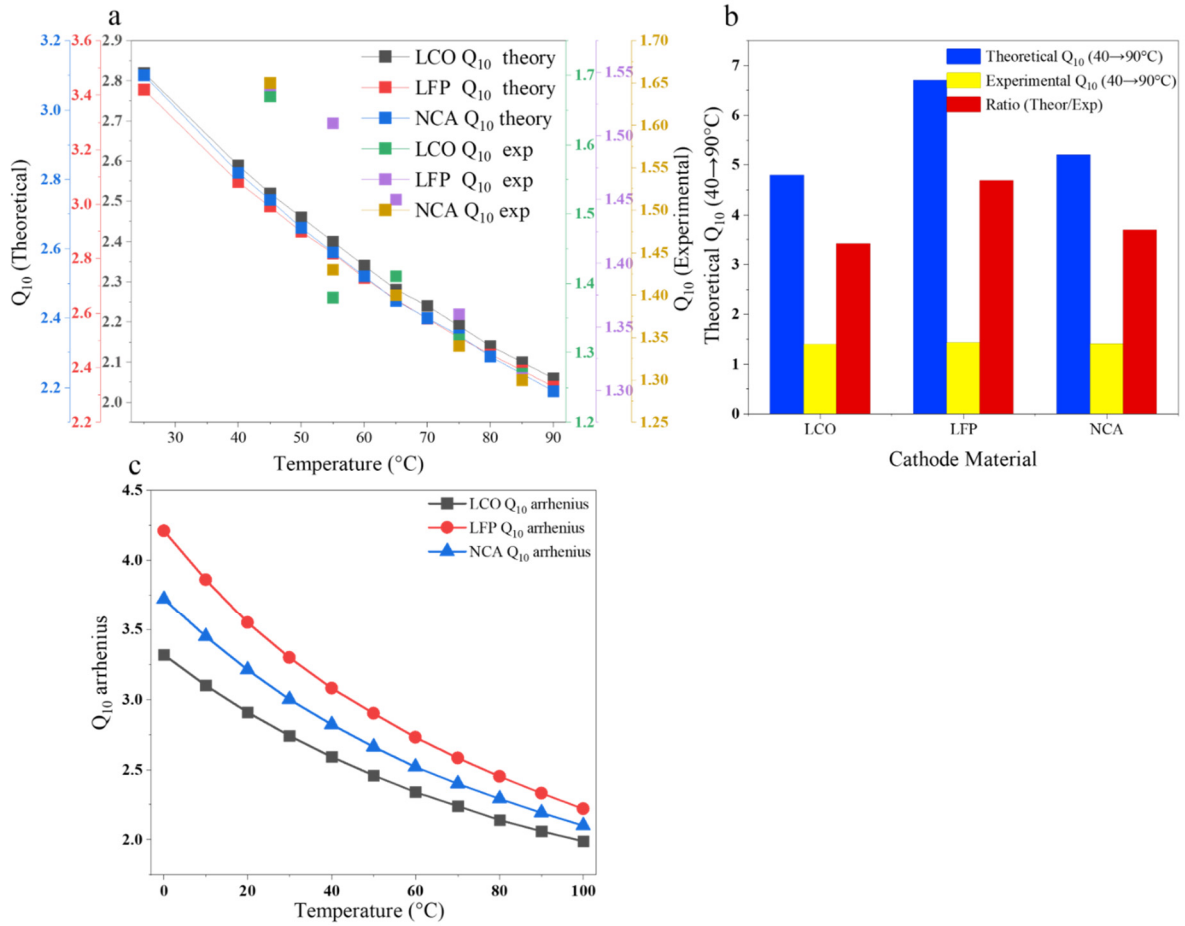

Figure 11. Temperature-dependent Q_{10} behavior of LCO, LFP, and NCA. (**a**) Theoretical and experimental Q_{10} values as a function of temperature, highlighting chemistry-specific thermal sensitivity. (**b**) Comparison of theoretical and experimental Q_{10} values over 40–90 °C, including theoretical-to-experimental ratios. (**c**) Arrhenius-derived Q_{10} values across a broad temperature range, showing activation-energy-driven differences among the three cathode materials.

3.4. Purification Logic and Product Quality of the Recovered Fractions

The selective separation of cathode active materials and aluminum current collectors achieves practical value only when the recovered fractions meet the purity requirements for subsequent material reuse. The TGA, SEM, EDXS, and XPS results in this work demonstrate that the ChelaDES process yields a pure black mass of high purity with minimum contamination with metallic foil. Moreover, the current collector, which is made of aluminum, is kept under conditions that allow direct reuse. This section presents the purification logic as an integrated strategy rather than a collection of separate observations, articulating the mechanistic basis for selective separation and quantifying the resulting product quality.

3.4.1. Purification Sequence Logic

The purification plan that was applied in this work was a definite step-by-step procedure. Selective interfacial weakening: ChelaDES entered the binder matrix and liaised with metal sites at the interface with the cathode-foil via hydroxamate-mediated chelation. This undermined the interfacial adhesion without attacking the active material or the aluminum foil to a large extent. Second, coating liberation from foil: Mild thermal treatment at temperatures up to 90 °C provided sufficient energy to disrupt the decreased adhesion and resulted in spontaneous or agitation-aided separation of the cathode coating on the foil surface. Third, for rinse-back recovery, vacuum filtration was used to collect the black mass on the surface of the foil and the treatment vessel. Fourth, residual solvent was removed. The remaining ChelaDES components of the recovered black mass were washed off with ethanol because of the difference in favorable solubility. Finally, the product was dried and sized. The refined black mass was dried to a constant weight and then graded to the required size (≤100 μm) for further hydrometallurgical treatment. This sequential logic ensures that each separation stage addresses specific impurity pathways, with the cumulative effect delivering the high-purity product documented in the characterization data.

3.4.2. Active Coating Removal Verification

TGA of untreated versus ChelaDES-treated cathode samples provides quantitative confirmation of effective coating removal through the principle of inverse proportionality between residual mass loss and removal efficiency. The untreated LCO exhibited a total mass loss of 17.3% across the 25–800 °C temperature range [28–30], with the major decomposition event (0.10%/°C peak) occurring at 225–275 °C and corresponding to PVDF binder decomposition. This is assumed to be consistent with oxygen release and phase transitions to Co_3O_4/CoO/metallic Co [28–31]. Following ChelaDES treatment at 90 °C for 60 min (93.7% removal efficiency), the mass loss of the treated LCO sample dramatically decreased to only 1.2%, with the DTG peak decreasing from 91–94% to 0.007%/°C. This reduction in thermal decomposition confirms that the mass loss observed in treated samples is attributable to residual coating rather than structural degradation of the recovered active material. LFP demonstrates the highest thermal stability among the untreated cathodes (3% total loss at 350 °C), which is consistent with the robust phosphate framework [32–35], and it has the lowest residual loss after treatment (0.3%), confirming effective liberation despite the threshold-limited kinetics. NCA, with the highest untreated mass loss (23%), shows a treatment-induced reduction to 1.8% loss, validating the transitional delamination behavior observed in kinetic studies [36–38].

Quantitative results of effective coating removal were found via TGA of the untreated and ChelaDES-treated cathodes. This has been interpreted on the basis of the inverse relationship between residual mass loss and removal efficiency. This study measured mass loss in relation to temperature (25–800 °C), which was due mainly to the loss of moisture (100–150 °C), decomposition of the binder/carbon (200–400 °C), and structural changes in the active material at higher temperatures [28–30]. To measure mass loss in the treated samples, the mass loss was scaled by the fraction of the coating remaining (1-average removal

percentage) under high-efficiency conditions (90 °C/60 min: 93.7% LCO, 90.8% LFP, 92.5% NCA) to indicate effective liberation of the active material without damaging the Al foil. Untreated samples exhibit a pronounced mass loss that reflects the entire coating composition, whereas the mass loss of the treated samples is minimal, indicating successful delamination and low residual degradation of the components [29,30]. In the case of LCO (untreated), a moderate total mass loss rate (17.3%) is observed, with a sharp decline between 150 and 300 °C (binder decomposition), which levels off to 82.7% at 400 °C (Figure 12a). This is assumed to be consistent with oxygen release and phase transitions to Co_3O_4/CoO/metallic Co [29–31]. In the case of LFP (untreated), the thermal stability is high, with a total loss of 3% at 350 °C, which increases progressively to 400 °C (minimal binder effect) (Figure 12b). This is consistent with the robust phosphate structure of LFP and oxidation at approximately 350–400 °C [32–35]. On the other hand, NCA caused the most significant mass loss (23%), with a sharp decrease in the 150–300 °C range (binder) and a gradual decrease to approximately 77% at 800 °C (Figure 12c). This may indicate the liberation of oxygen and the transformation of the phase to spinel/rock salt structures [36–38]. The mass loss of the treated samples decreased to approximately 0.3–1.8%, with almost flat curves after the loss of moisture, confirming over 90% removal and a minor residual coating [31]. The stabilities of the materials differ in this order (LFP > LCO > NCA) for the loss of untreated cathodes, indicating that ChelaDES is effective in maintaining foil and eliminating coatings [36,37]. The curves obtained after ChelaDES treatment converge toward high retention, and the best removal is provided by LCO, resulting in a flat profile (Figure 12a).

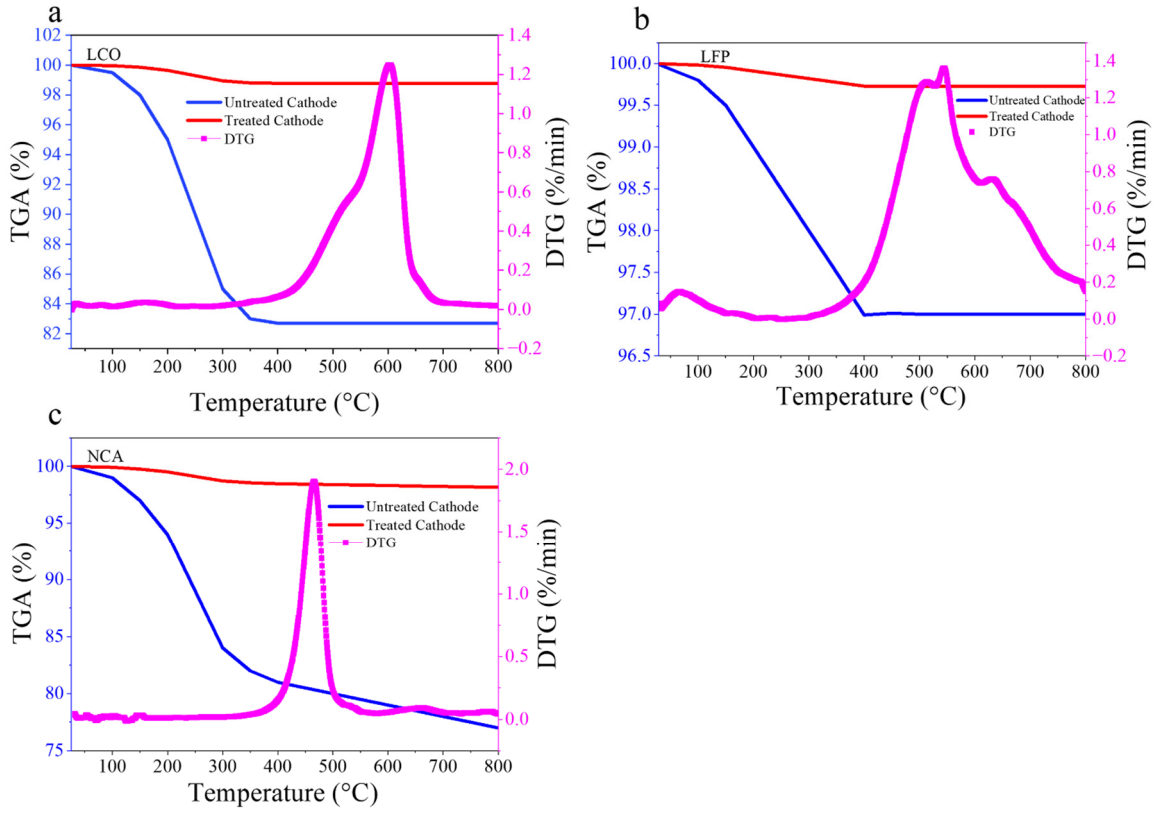

Figure 12. TGA-DTG profiles of the untreated and ChelaDES-treated cathodes showing the characteristic thermal decomposition behavior of (**a**) LCO, (**b**) LFP, and (**c**) NCA.

3.4.3. Foil Preservation Assessment

The integrity of aluminum current collectors is also of paramount importance to the success of the process because the damage to the foil would create metal contamination in the black mass and prevent the reuse of the foil. XPS depth profiling of post-treatment LCO surfaces (10 nm sampling depth) revealed that

the Al 2p signal intensities increased from 10 arbitrary units (undetectable) in the untreated coated state to 100 arbitrary units after treatment, and the Co 2p signal decreased by 100–5.6% of its original value (Figure S7a). This reversal of the intensities of the signals, in which Al is the dominant surface component, and Co decreases to trace levels, confirms total or nearly total elimination of the active coating with no trace of Al dissolution or pitting. The similar decrease in the C 1 s (PVDF binder) and F 1 s signals to 4.2% of the original values is additional evidence that the separation process takes place at the coating–foil interface without further penetration into the foil substrate and disintegration (Figure S7).

3.4.4. Cross-Contamination Control

Mapping the recovered black masses of all three cathode chemistries via EDXS reveals that minimal carryover of current collector metals occurs. This establishes the efficacy of the interfacial selectivity mechanism. In the case of the black mass of LCO (Figure 13a), the EDXS spectrum shows the presence of Co and O signals with no evidence of Al or Cu above the instrumental detection limit, thus supporting less than 0.1 wt% contamination of the metallic foil. The LFP-derived black mass (Figure 13b) has a dominant Fe and P signal with some traces of Al, which is in line with the XPS findings of the remaining PVDF remaining at the foil interface and not metallic dissolution. The NCA-derived black mass (Figure 13c) indicates the anticipated Ni and Co traces with only minor Al traces, which suggests that the mixed-metal structure of the active material is free of impurities with no cross-contamination of the Al or Cu current collectors.

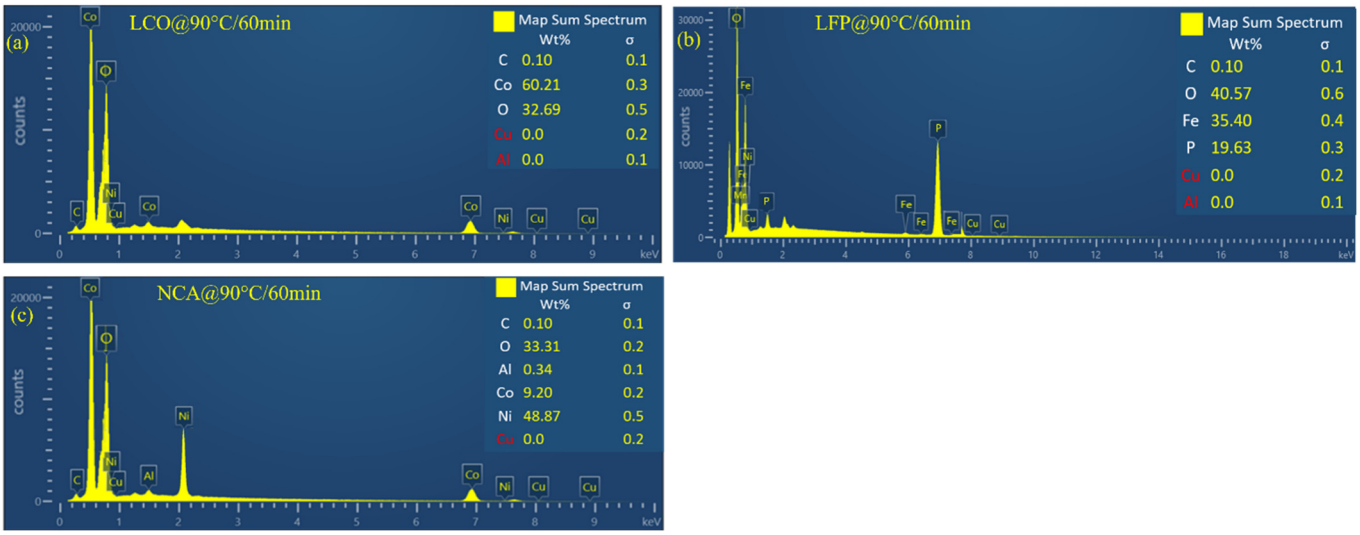

Figure 13. Energy dispersive X-ray spectroscopy (EDXS) analysis of three different cathode materials under specified conditions (90 °C/60 min): (**a**) LCO, (**b**) LFP, and (**c**) NCA.

3.4.5. Process Consistency and Reproducibility

SEM morphological analysis (Figure 14) provides visual confirmation of the purification mechanism, revealing distinct surface transformations that are consistent with selective interfacial failure rather than bulk material degradation. LCO treated at 90 °C for 60 min resulted in isolated platelet particles with distinct edges and no residual binder films, characteristic of complete delamination. LFP treated under the same conditions shows dispersed prismatic particles with surface pitting, which is consistent with interfacial disruption at the phosphate-binder interfaces. The NCA shows fragmented particles with low adhesive forces, which is consistent with the transitional delamination mechanism. The morphological preservation of particle integrity across all three chemical methods indicates that the purification process does not induce mechanical damage or structural transformation, which would compromise the value of the recovered active materials for subsequent downstream processing.

Visual validation of the purification mechanism via SEM morphological analysis (Figure 14) revealed that specific surface changes occur and are consistent with selective interfacial failure, as opposed to bulk material degradation. SEM provides a detailed view of the topography and morphological features of the surface, which is critical evidence of the delamination process caused by ChelaDES. This method confirms gravimetric trends, including the percentage removal percentage that increases with temperature, and indicates individual interfacial chemical disturbances. The products of post-delamination SEM, however, vary on the basis of the degree of liberation and the material that is left behind.

In the case of lithium cobalt oxide (LCO), where the delamination efficiency is progressive (93.7% removal at 90 °C in 60 min), SEM images reveal that the particles are uniformly released. At lower temperatures (approximately 53% removal), flaky platelets (10–20 μm) are still closely packed with unbroken binder networks [9] (Figure 14a). At moderate temperatures, partial flaking and the formation of cracks along the boundaries of the particles are noted, which is a sign of the first chelation (Figure 14b). Higher temperatures are characterized by isolated platelets with distinct edges that dominate the SEM image, which corroborates the near-total delamination shown in Figure 14c. The exposed surfaces exhibit minimal residual films, indicating efficient penetration of ChelaDES into the PVDF–particle network. Correspondingly, EDXS mapping confirmed the dominance of Co and O signals with negligible Al or Cu (Figure 13a), demonstrating that delamination proceeded without foil abrasion or contamination.

SEM revealed the threshold behavior of lithium iron phosphate (LFP), with negligible removal at 60 °C for 40 min and 90.8% removal at 90 °C for 60 min. At lower temperatures, the small, rod-like clusters (1–10 μm) are coated with fuzzy carbon layers, and nothing is visibly disturbed (Figure 14d). At higher temperatures, little separation and the appearance of sharp cracks can be observed when the temperature exceeds the threshold temperature (Figure 14e). The presence of dispersed prisms that have surface pitting through the disruption of phosphates is the result of high-efficiency delamination, which thus verifies the integrity of the black mass (Figure 14f). The EDXS spectra corroborate this behavior, showing high Fe and P intensities with no detectable Al (Figure 13b), confirming that even under threshold-driven delamination, the aluminum substrate remains fully preserved.

The delamination acceleration of nickel co-orbital aluminum (NCA) is transitional (92.5% removal at 90% for 60 min), as evidenced by SEM images showing morphologies that change under different conditions. At lower temperatures, small spherical aggregates (20–30 μm) with textured surfaces are observed (Figure 14g). Under intermediate conditions, partial disassembly and peeling of the nickel-rich layers occur (Figure 14h). At elevated temperatures, dispersed fragments with low adhesive forces are found, which is consistent with the kinetic data obtained for this material (Figure 14i). EDXS mapping reveals dominant Ni and Co signals with only trace Al, indicating that ChelaDES effectively removes the active layer while avoiding foil dissolution (Figure 13c). The slight heterogeneity in particle morphology aligns with the kinetic data, which show gradual acceleration rather than abrupt threshold behavior.

Collectively, the SEM–EDXS results confirm that ChelaDES achieves chemistry-specific delamination while maintaining high black-mass purity. The absence of Al and Cu residues across all the spectra confirms that the solvent selectively disrupts the binder–cathode interface without attacking the current collector, supporting its suitability for direct recycling workflows. The morphological stability of the particle structure in all three chemical methods implies that the purification procedure does not cause mechanical or structural changes that may cause degradation of the value of the active materials recovered to be resynthesized.

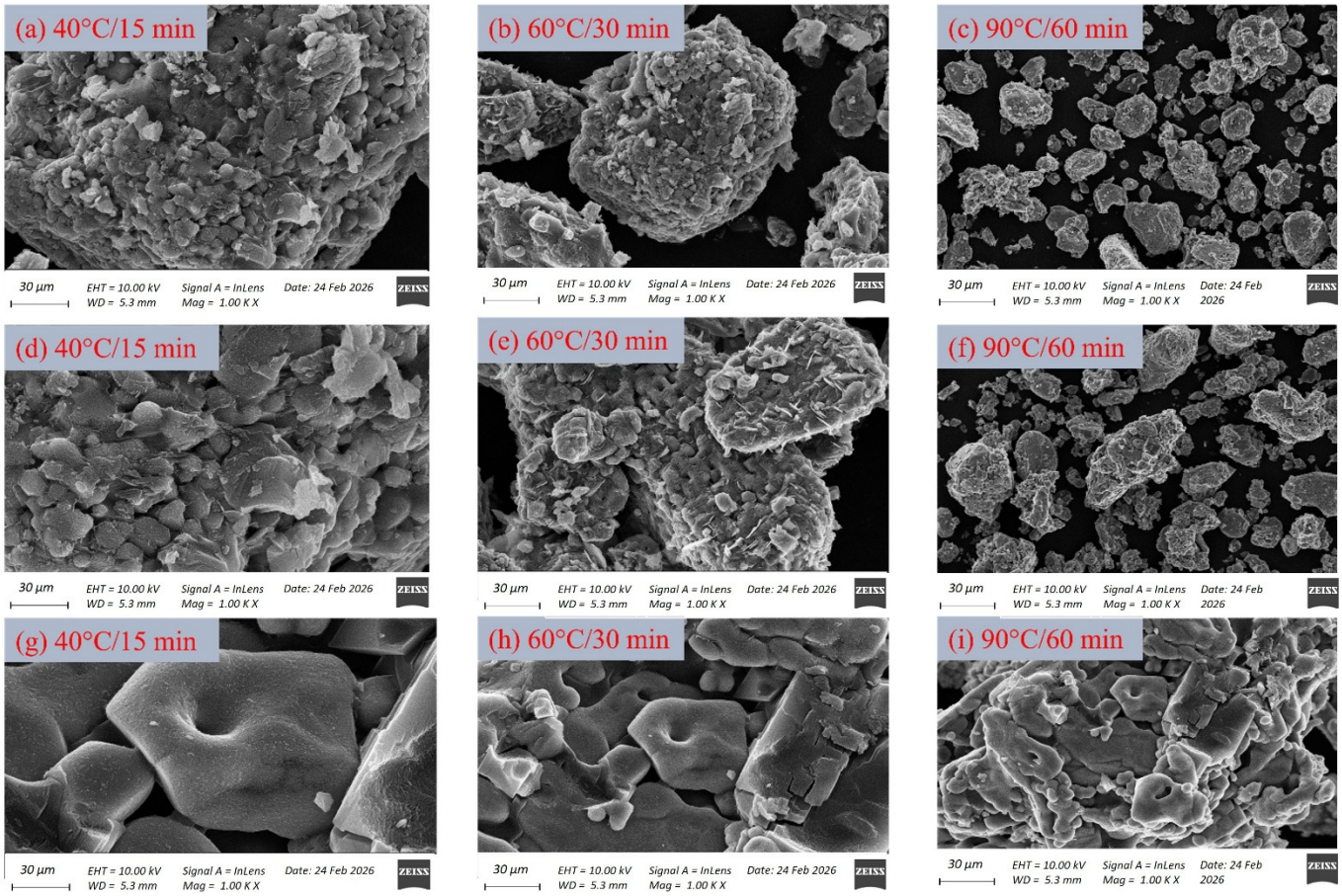

Figure 14. SEM micrographs illustrating the evolution of the cathode-particle morphology during ChelaDES delamination with increasing treatment severity: (**a**–**c**) LCO, (**d**–**f**) LFP, and (**g**–**i**) NCA, each shown at 40 °C/15 min, 60 °C/30 min, and 90 °C/60 min, respectively, highlighting progressive interfacial disruption and particle liberation with increasing temperature and time.

3.5. Process Mechanism and Engineering Implications

The kinetic modeling findings in this study are used to explain processes other than competing with the main process outcomes reported in Sections 3.1–3.3. The four complementary models, which include pseudo-first-order (PFO), pseudo-second-order (PSO), Avrami, and Fickian diffusion, constitute a mechanistic framework for rationalizing the chemistry-dependent separation windows and defining the basic parameters needed to design and scale up the process. The main finding of this modeling work is that ChelaDES-mediated selective separation is a thermally activated, transport-limiting interfacial softening mechanism, the kinetics of which are regulated by the diffusion of chelator components across the binder matrix and by the weakening of interfacial bonds between metals and binders through coordination.

3.5.1. Fickian Diffusion as the Rate-Controlling Mechanism

The Fickian diffusion model [39,40], which was developed to consider slab geometry, is the most physical model that describes separation kinetics, as attested by the superior fits to the sigmoidal removal profiles (LCO $R^2 = 0.97$, LFP and NCA $R^2 = 0.95$) (Figure 15). In this model, the penetration of ChelaDES, which is assumed to be a thin film, through the cathode coating, through which it diffuses, is assumed to be an effective half-thickness L. Consequently, the coordination of binder-metal interfaces is broken by hydroxamate coordination, and the active material is gradually released. The removal fraction $f(t)$, which represents the proportion of active material delaminated as a function of time t, asymptotically approaches 1, indicating complete removal.

Fits were performed via averaged replicate data for each material and temperature range (40–90 °C), employing nonlinear least-squares optimization. The model is a good representation of the sigmoidal kinetics that are defined by a rapid growth of $f(t)$ during the early stages of diffusion (diffusion-dominated) and an asymptotic approach to full delamination. The model also offers quite reasonable fits in cases where there is negligible removal at early times (LFP at low temperatures). However, the sudden onset indicates that induction periods (threshold coordination energy) might be present.

The fitted parameters of each material demonstrate that LCO has the quickest delamination at all temperatures and high initial removal (53% at 40 °C/15 min, nearly 94% at 90 °C/60 min) (Figure 15a). The low E_a (19.51 kJ/mol) value means that ChelaDES diffusion and coordination have a low energy barrier and can be effectively used under mild conditions (40–60 °C) (Figure 15d). This implies that the Cobinder interfaces are efficiently disrupted by the formation of hydroxamic acids, which may form stable octahedral complexes with Co^{3+} and rapidly weaken adhesion. On the other hand, LFP has a slow onset, and its removal is insignificant at low temperatures/times (0% at 40 °C for 40 min but 71% at 50 min) (Figure 14b). Then, it increases with temperature (91% at 90 °C/60 min). The large E_a (39.50 kJ/mol) is a sign of a strong dependence on temperature, probably because of less coordination of Fe^{3+} with hydroxamates or a denser olivine structure that prevents diffusion (Figure 15d). The large A factor indicates compensated entropy, so it can undergo kinetics quickly once it is activated (>70 °C). NCA exhibited intermediate behavior, with moderate initial removal (0% at 40 °C for 15–30 min but 53% at 40 min), and steadily progressed at 90 °C for 60 min (93%) (Figure 15c). Moreover, the E_a of NCA (28.84 kJ/mol) is between those of LCO and LFP, presumably as a result of the mixed Ni/Co/Al sites; Ni^{2+}/Co^{3+} ions coordinate well with hydroxamates, whereas Al^{3+} ions produce weaker complexes, resulting in balanced but slower diffusion than LCO (Figure 15d).

The order of the relationships among the materials is LCO > NCA > LFP in terms of the total delamination rate, which is associated with the hydroxamate affinity (Co > Ni/Co/Al > Fe). The thermal control of ChelaDES is most evident in LFP, where an extreme change from inert to reactive takes place at temperatures above 60 °C. This may enable the selective processing of mixed cathode streams. The activation energy hierarchy (LFP > NCA > LCO) shows that ChelaDES is selective: the low E_a for Co-rich materials is consistent with the reported effectiveness of levulinyl hydroxamic acid in the recovery of Co/Mn/Ni in LIB black masses (Figure 15d). The large E_a for LFP could be caused by the competition of phosphate groups with coordination or increased cohesion of the binder in olivine cathodes. The pre-exponential factors (A) tend to be LFP > NCA > LCO, indicating that there is more configurational freedom in LFP after the barrier has been overcome. This is probably because polyol (C-OMe/GA) components are better solvated in Fe environments. These disparities support the design of ChelaDES as a specific system, in which green coordination is encouraged by the bioderived nature of LH (a product of levulinic acid) and provides adequate interfacial coordination, leading to delamination.

The pseudo-first-order and pseudo-second-order methods further provide a comprehensive framework for understanding the delamination of cathode materials by ChelaDES. The findings of the PSO model are similar to those of the diffusion model for the majority of materials, which means that the delamination rate is more complicated than originally considered in the PFO model (Figures S8 and S9). Future optimization, such as adjusting the LH:GA ratio, could lower the LFP's E_a for more uniform performance across chemistries.

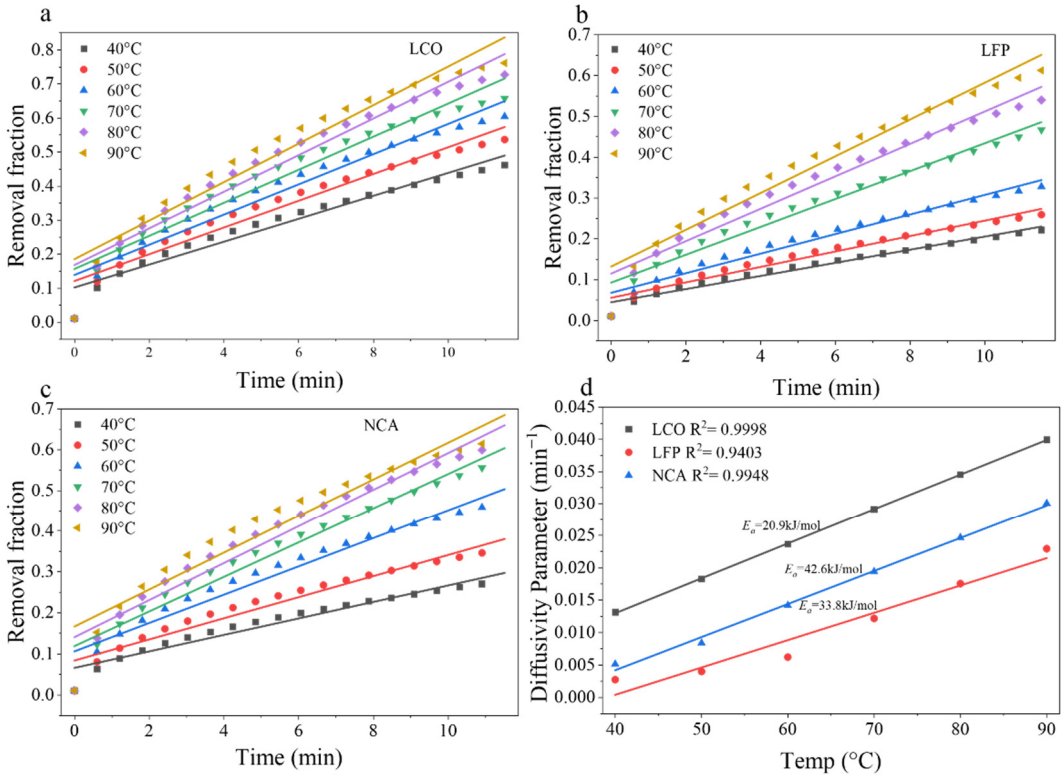

Figure 15. Fickian-diffusion modeling of ChelaDES delamination kinetics for LCO, LFP, and NCA. (**a**) LCO removal fraction (0–60 min, 40–90 °C) showing that temperature-accelerated sigmoidal behavior. (**b**) LFP removal fraction with clear induction delays at lower temperatures. (**c**) The NCA removal fraction exhibited intermediate kinetics across the same temperature range. (**d**) Arrhenius-derived diffusion activation energies (E_a) for all three cathode chemistries.

3.5.2. Interfacial Softening and Hydroxamate Coordination

The Avrami kinetic analysis [41] can be used to complement the mechanistic understanding by identifying the delamination regimes that are dominated by nucleation and diffusion-limited regimes. In the case of LCO, the kinetics of delamination are fast, which is explained by the low activation energy (25.5 kJ/mol) of the process, indicating that it is dominated by nucleation. This is in line with the acceleration and then saturation tendency in the delamination profiles, as shown by the steep Avrami slope in Figure 16a. The k_{LCO} is nearly two or three times greater than the k_{NCA} and 4–6 times greater than the k_{LFP}. The large value of R^2 (>0.97) confirms a very good fit with the model. The kinetics of LCO indicate that more than 90% of the active material is eliminated in the first 60 min. Accordingly, the corresponding largest Avrami exponent (n_{LCO}) and rate constant (k_{LCO}) are used.

Conversely, LFP has threshold-dependent delamination behavior, which means that it takes more temperature (≥60 °C) to start removing the material significantly. The lower Avrami exponent of LFP is an indication of this threshold effect, as diffusion-limited kinetics are implied by the strength of the binder material preventing delamination at lower temperatures. This is supported by the Arrhenius analysis (Figure 16b), in which LFP has a higher activation energy (28.5 kJ/mol), which is associated with the energy needed to break the chemical and structural resistance of the Fe–P–O binder network.

The hybrid character of the delamination mechanism of NCA is emphasized by the intermediate nature of the behavior. A shift in the activation temperature to approximately 60 °C is an indication of a change between diffusion-limiting and nucleation-limiting processes. This transitional behavior is manifested by the Avrami exponent of NCA in Figure 16c, in which the process needs to be fed more thermal input than LCO but less thermal input than LFP to reach a 92% removal fraction. This behavior is in line with the intermediate activation energy (26.5 kJ/mol) of NCA and indicates that the Ni-rich layered oxide surfaces

are affected by thermally activated interfacial weakening, which is highly affected by hydroxamate coordination. The differences in the activation energy and threshold behavior experimentally observed are explained by the chemistry-specific coordination affinities (Co > Ni/Co/Al > Fe).

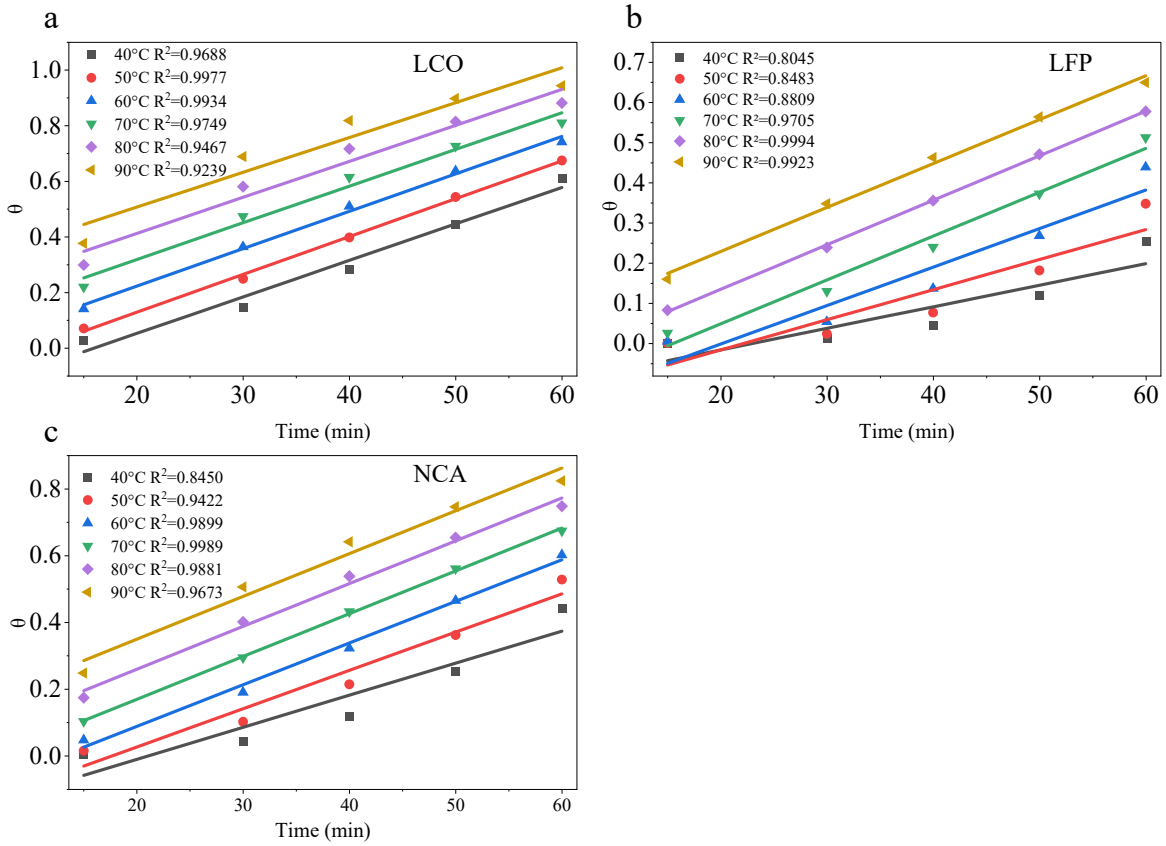

Figure 16. Avrami analysis of delamination kinetics for LCO, LFP, and NCA. (**a**) LCO shows a high Avrami exponent, indicating rapid, multidimensional interfacial transformation. (**b**) LFP has the lowest exponent, which is consistent with slow, diffusion-limited delamination. (**c**) NCA displays an intermediate response, reflecting a mixed mechanism with moderate interfacial softening and partial diffusion constraints.

3.5.3. Engineering Implications for Scale-Up Processes

The kinetic parameters used in this research provide the basic foundation for process scale-up calculations. The PSO model gave the most satisfactory overall account of the temporal evolution of the removal fraction (R^2 = 0.978–0.992 for all chemistries and at all temperatures) (Figure S8). This gives rate constants that depend on temperature in the Arrhenius relationship (Figure S9). To be used in reactor design, the characteristic time to 90% separation (t_{90}) can be determined as $t_{90} = 1/(k_2 \times 0.9)$, and one can easily compare process throughput under operating conditions. At 90 °C, the t_{90} values are approximately 15 min (LCO), 20 min (NCA), and 25 min (LFP). This suggests that with an optimized residence time of 30 min, a single reactor stage would be able to achieve more than 90% liberation efficiency. The transport-limited character of the mechanism has significant consequences for receptor design and mixing. The external mass transfer to the electrode surface should be strong enough to be sustained close to the saturation concentration of the ChelaDES components at the coating surface. This mixture is maintained in laboratory experiments by agitation at 300 rpm. The need to scale up to industrial-level batches or continuous reactors will consider the power input per unit volume and the agitator design to achieve the proper mixing intensity without causing mechanical damage to the delicate separated coating. The diffusion-controlled kinetics also presuppose that the characteristic time varies with the square of the coating thickness ($t \propto L^2$) so that the

optimization of the process to obtain thicker electrode coatings will require longer residence times or increased driving forces (higher temperatures or ultrasonic-aided diffusion).

The selective interfacial separation process reported in this study has a rare set of properties: high separation efficiency (>90%), high selectivity (Al/Cu < 0.1 wt% in black mass), foil preservation (Al signal inversion in XPS), and low energy requirements (90 °C operation), which make this process unique among traditional recycling methods. Pyrometallurgical processes are effective in extracting metals, but they destroy the cathode microstructure and require temperatures greater than 1000 °C, with energy usage and emissions. Hydrometallurgical leaching is a selective method of recovering metals, although it produces acidic waste and corrodes existing collectors, lowering the value of the material. By functioning at the cathode-foil interface, where selective coordination chemistry instead of bulk dissolution occurs, the ChelaDES process maintains material integrity and allows recovery of the cathode active material and foil preservation. This is vital to achieve the true findings of a circular economy in lithium-ion battery recycling.

4. Conclusions

ChelaDES was a good low-temperature stationary phase for the selective interfacial separation of spent LIB cathodes. This allowed the liberation of foil without an obvious bulk attack on the Al current collector and generated a black mass that could be recovered as low-impurity black mass. LCO was the most responsive, with 93.7% active material removal and >99% bare-Al exposure at 90 °C for 60 min. NCA was intermediate, and LFP displayed a response that was controlled at the threshold and required more severe conditions. Closely monitored bare-Al exposure tracked the mass per unit area, demonstrating its value as a practical metric for separation quality. Additional purification findings revealed negligible carryover values of Al/Cu and low residual coating and intact foil integrity. On the whole, selective interfacial weakening, rather than bulk dissolution, controls the process, making ChelaDES a promising platform for direct battery recycling that integrates mild operating conditions, chemistry-specific process control, foil preservation, and high-purity black-mass recovery.

Supplementary Materials

The following supporting information can be found at: https://www.sciepublish.com/article/pii/1134, Figure S1: ^{1}H NMR of Trimethyl(2-methoxyethyl) Ammonium Chloride (C-OMe); Figure S2: Synthesis of glyceric acid; Figure S3: Synthesis of ternary ChelaDES (LH:C-OMe:GA); Figure S4: Time-lapse visual comparison of delamination behavior for LCO (a), LFP (b), and NCA (c) cathodes immersed in ChelaDES from 15 to 60 min, illustrating chemistry-dependent differences in coating dissolution, dispersion, and interfacial weakening; Figure S5: Representative ImageJ outputs for bare Al quantification on LCO at 40 °C/15 min. (a) Results summary table showing 91 exposed regions (9.2% area, mean intensity 254.8). (b,c) Binary thresholded masks highlighting segmented Al particles (white) amid coated regions (black), with particle outlines for verification. Scale bar: 1 cm; Figure S6: Time-lapse photographs of cathode delamination in ChelaDES; Figure S7: Comparative XPS peak intensities at selected binding energies for (a) LCO, (b) LFP, and (c) NCA before and after delamination at 90 °C for 60 min; Figure S8: Kinetic model evaluation for temperature-dependent reaction progress in LCO, LFP, and NCA. (a,b) Pseudo-second-order (PSO) and pseudo-first-order (PFO) fits for LCO, showing temperature-enhanced kinetics and model-dependent linearization. (c,d) PFO and PSO fits for LFP, with improved linearity and faster kinetics under the PSO model. (e,f) PFO and PSO analyses for NCA, demonstrating strong linearity and temperature-driven rate acceleration, particularly under the PSO framework; Figure S9: Arrhenius analysis of temperature-dependent rate constants for LCO, LFP, and NCA. (a) Pseudo-first-order Arrhenius plots showing linear $\ln(k_1)$–$1/T$ relationships with strong fit quality across all three chemistries. (b) Pseudo-second-order Arrhenius plots displaying similarly high linearity in $\ln(k_2)$–$1/T$, confirming thermally

activated kinetics consistent with Arrhenius behavior; Table S1: Summary Statistics of delamination data from LCO, LFP and NCA cathode material; Table S2: Pearson Correlation Analysis; Table S3: Activation energies (E_a) for delamination; Table S4: Key Metrics Linking TGA and Removal; Table S5: ANOVA Summary for Removal Percentage (%) at 60 Minutes Across Temperatures (40–90 °C); Table S6: Combined Tukey's HSD Pairwise Comparisons for All Temperatures; Table S7: Combined Two-Way ANOVA Summary for Time Effects (Time × Chemistry per Temperature); Table S8: Tukey's HSD Pairwise Comparisons for Time Effects (Main Effect of Time per Temperature); Table S9: Tukey's HSD Pairwise Comparisons for Interaction Effects (Time × Chemistry per Temperature).

Statement of the Use of Generative AI and AI-Assisted Technologies in the Writing Process

During the preparation of this manuscript, the authors used generative AI and AI-assisted technologies solely for language refinement, grammatical correction, and improvement of textual clarity and readability. These tools were not used to generate experimental data, perform data analysis, interpret results, formulate scientific conclusions, or create the underlying scientific content of the study. All AI-assisted text was critically reviewed, verified, and revised by the authors, who take full responsibility for the accuracy, integrity, originality, and final content of the manuscript.

Acknowledgments

The authors gratefully acknowledge Scientific Compass (www.shiyanjia.com) for providing technical support and assistance with materials characterization.

Author Contributions

P.A.: writing—original draft, methodology, visualization, data curation, formal analysis, investigation, software. Z.Q.: writing—original draft, methodology, visualization, data curation, formal analysis, investigation, software; L.G.: funding, conceptualization, supervision, writing—review and editing, and validation. M.T.: data curation, formal analysis, investigation.

Ethics Statement

Not applicable. This study did not involve human participants, human biological materials, identifiable personal data, or animals. Therefore, ethical approval was not required.

Informed Consent Statement

Not applicable. This study did not involve human participants or the collection of personal or identifiable information; therefore, informed consent was not required.

Data Availability Statement

The datasets generated and analyzed during this study are available in the supplementary and are openly available in the Mendeley Data repository: Afreh Paul, Zhiqin Qin, Lizhen Gao (2026), "Thermally Driven Cathode Delamination in Lithium-Ion Batteries: Experimental Data on LCO, LFP, and NCA Chemistries", Mendeley Data, V1, DOI:10.17632/5rpmg2xm3t.1.

Funding

The author(s) disclosed receipt of the following financial support for the research, authorship, and/or publication of this article: This work was supported by the Shanxi Provincial Department of Education under project name "Science and Technology Innovation Base" [grant number: YDZJSX20231B002].

Declaration of Competing Interest

The authors declare that they have no known competing financial interests or personal relationships that could have appeared to influence the work reported in this paper.

References

1. Dong Y, Ji H, Wu X, Zheng N, Wang J, Ji G, et al. Trends of sustainable recycling technology for lithium-ion batteries: Metal recovery from conventional metallurgical processes to innovative direct recycling. *MetalMat* **2024**, *1*, e5. DOI:10.1002/metm.5
2. Reck BK, Graedel TE. Challenges in Metal Recycling. *Science* **2012**, *337*, 690–695. DOI:10.1126/science.1217501
3. Lo Sardo C, Cacciatore G, Cappuccino G, Aiello D, Napoli A. Spent Lithium Battery Recycling: Traditional and Innovative Approaches. *Processes* **2025**, *13*, 950. DOI:10.3390/pr13040950
4. Zheng X, Zhu Z, Lin X, Zhang Y, He Y, Cao H, et al. A Mini-Review on Metal Recycling from Spent Lithium Ion Batteries. *Engineering* **2018**, *4*, 361–370. DOI:10.1016/j.eng.2018.05.018
5. Buken O, Mancini K, Sarkar A. A sustainable approach to cathode delamination using a green solvent. *RSC Adv.* **2021**, *11*, 27356–27368. DOI:10.1039/d1ra04922d
6. Xue Z, Yu D, Zhao X, Mu T. Upgrading of levulinic acid into diverse N-containing functional chemicals. *Green Chem.* **2019**, *21*, 5449–5468. DOI:10.1039/C9GC02415H
7. Padwal C, Pham HD, Jadhav S, Do TT, Nerkar J, Hoang LTM, et al. Deep Eutectic Solvents: Green Approach for Cathode Recycling of Li-Ion Batteries. *Adv. Energy Sustain. Res.* **2022**, *3*, 2100133. DOI:10.1002/aesr.202100133
8. Tran MK, Rodrigues MTF, Kato K, Babu G, Ajayan PM. Deep eutectic solvents for cathode recycling of Li-ion batteries. *Nat Energy* **2019**, *4*, 339–345. DOI:10.1038/s41560-019-0368-4
9. Cattaneo P, Callegari D, D'Aprile F, Quartarone E. A sustainable delamination approach for simultaneous separation and leaching of cathodes from end-of-life Li ion batteries. *J. Power Sources Adv.* **2025**, *34*, 100181. DOI:10.1016/j.powera.2025.100181
10. Somo TR, Mabokela TE, Teffu DM, Sekgobela TK, Ramogayana B, Hato MJ, et al. A Comparative Review of Metal Oxide Surface Coatings on Three Families of Cathode Materials for Lithium Ion Batteries. *Coatings* **2021**, *11*, 744. DOI:10.3390/coatings11070744
11. Citarella A, Moi D, Pinzi L, Bonanni D, Rastelli G. Hydroxamic Acid Derivatives: From Synthetic Strategies to Medicinal Chemistry Applications. *ACS Omega* **2021**, *6*, 21843–21849. DOI:10.1021/acsomega.1c03628
12. Goudarzi J, Chen Z, Zhang G, Hu J, Zaghib K, Deng S, et al. Sustainable Recovery of Critical Metals from Spent Lithium-Ion Batteries Using Deep Eutectic Solvents. *Batteries* **2025**, *11*, 340. DOI:10.3390/batteries11090340
13. Hayagan N, Aymonier C, Croguennec L, Morcrette M, Dedryvère R, Olchowka J, et al. A holistic review on the direct recycling of lithium-ion batteries from electrolytes to electrodes. *J. Mater. Chem. A* **2024**, *12*, 31685–31716. DOI:10.1039/D4TA04976D
14. Xia Y, Meng F, Xiao Y, Nie S, Lin W, Han Q, et al. Recent Advances on Eco-Friendly Techniques on Separating Active Materials from Current Collectors in Spent Lithium-Ion Batteries. *ACS Appl. Mater. Interfaces* **2025**, *17*, 50087–50102. DOI:10.1021/acsami.4c21822
15. Pang D, Wang H, Zeng Y, Han X, Zheng Y. Sustainable Recycling of Lithium-Ion Battery Cathodes: Life Cycle Assessment, Technologies, and Economic Insights. *Nanomaterials* **2025**, *15*, 1283. DOI:10.3390/nano15161283
16. Wang J, Wang Y, Lyu Y, Mao J, Guo Z. Stage-Specific Roles of Deep Eutectic Solvents in Recycling of Spent Lithium-Ion Batteries. *Adv. Energy Mater.* **2026**, *16*, e06741. DOI:10.1002/aenm.202506741
17. Abbott AP, Capper G, Davies DL, Rasheed RK, Tambyrajah V. Novel solvent properties of choline chloride/urea mixtures. *Chem. Commun.* **2003**, *39*, 70–71. DOI:10.1039/b210714g
18. Smith EL, Abbott AP, Ryder KS. Deep Eutectic Solvents (DESs) and Their Applications. *Chem. Rev.* **2014**, *114*, 11060–11082. DOI:10.1021/cr300162p
19. Zhang Q, De Oliveira Vigier K, Royer S, Jérôme F. Deep eutectic solvents: Syntheses, properties and applications. *Chem. Soc. Rev.* **2012**, *41*, 7108. DOI:10.1039/C2CS35178A
20. Paiva A, Craveiro R, Aroso I, Martins M, Reis RL, Duarte ARC. Natural Deep Eutectic Solvents—Solvents for the 21st Century. *ACS Sustain. Chem. Eng.* **2014**, *2*, 1063–1071. DOI:10.1021/sc500096j
21. Li L, Zhang X, Li M, Chen R, Wu F, Amine K, et al. The Recycling of Spent Lithium-Ion Batteries: A Review of Current Processes and Technologies. *Electrochem. Energy Rev.* **2018**, *1*, 461–482. DOI:10.1007/s41918-018-0012-1

22. Yan T, Wang H, Zhong S, Ma Q, Nie W, Guo X, et al. Thermal decomposition mechanisms and strategies for enhancing fluorine removal from polyvinylidene fluoride binders in Li-ion battery cathode materials. *Mater. Today Commun.* **2025**, *49*, 113824. DOI:10.1016/j.mtcomm.2025.113824
23. Harper G, Sommerville R, Kendrick E, Driscoll L, Slater P, Stolkin R, et al. Recycling lithium-ion batteries from electric vehicles. *Nature* **2019**, *575*, 75–86. DOI:10.1038/s41586-019-1682-5
24. Liu S, Dong C, Che S, Ma G, Cheng G, Tian Y, et al. Graphene-coated current collectors for enhanced interfacial stability and electrochemical performance in $LiFePO_4$||Li batteries. *Electrochim. Acta* **2025**, *540*, 147231. DOI:10.1016/j.electacta.2025.147231
25. He FR, Tian ZQ, Xiang W, Yang W, Zheng BP, Cai JY, et al. Insight into the Surface Reconstruction-Induced Structure and Electrochemical Performance Evolution for Ni-Rich Cathodes with Postannealing after Washing. *ACS Appl. Mater. Interfaces* **2023**, *15*, 9160–9170. DOI:10.1021/acsami.2c15909
26. Baunach M, Jaiser S, Schmelzle S, Nirschl H, Scharfer P, Schabel W. Delamination behavior of lithium-ion battery anodes: Influence of drying temperature during electrode processing. *Dry. Technol.* **2016**, *34*, 462–473. DOI:10.1080/07373937.2015.1060497
27. Liang L, Zhang W, Zhao F, Denis DK, Zaman FU, Hou L, et al. Surface/Interface Structure Degradation of Ni-Rich Layered Oxide Cathodes toward Lithium-Ion Batteries: Fundamental Mechanisms and Remedying Strategies. *Adv. Mater. Interfaces* **2020**, *7*, 1901749. DOI:10.1002/admi.201901749
28. Veluchamy A, Doh CH, Kim DH, Lee JH, Shin HM, Jin BS, et al. Thermal analysis of Li_xCoO_2 cathode material of lithium ion battery. *J. Power Sources* **2009**, *189*, 855–858. DOI:10.1016/j.jpowsour.2008.07.090
29. Windisch-Kern S, Holzer A, Ponak C, Hochsteiner T, Raupenstrauch H. Thermal analysis of lithium ion battery cathode materials for the development of a novel pyrometallurgical recycling approach. *Carbon Resour. Convers.* **2021**, *4*, 184–189. DOI:10.1016/j.crcon.2021.04.005
30. Yang Y, Gao Y, Miao Y, Liang Y, Ren X. Research Progress on the Influence of Cathode Materials on Thermal Runaway Behavior of Lithium-Ion Batteries. *Batteries* **2025**, *11*, 373. DOI:10.3390/batteries11100373
31. Janisse A. Thermal Degradation and Evolved Gas Analysis of Lithium-Ion Battery Cathode Materials at Different States of Charge—TA Instruments. Available online: https://www.tainstruments.com/applications-notes/thermal-degradation-and-evolved-gas-analysis-of-lithium-ion-battery-cathode-materials-at-different-states-of-charge-ta495/ (accessed on 20 February 2026).
32. Feng E, Li P, Huang Z, Zan W, Wang T, Ren Z, et al. Ultrafast Material Separation by Electrochemical Delamination for Spent Lithium-Ion Batteries Recycling. *ACS Sustain. Chem. Eng.* **2025**, *13*, 16872–16883. DOI:10.1021/acssuschemeng.5c06070
33. Ji Y. Sustainable Delamination of Cathode Materials from Spent Lithium-Ion Batteries. Ph.D. Thesis, Purdue University Graduate School, West Lafayette, IN, USA, 2022.
34. Mehrotra A, Berwal P, Lee Y, Yoh JJ. Anode-triggered thermal runaway in $LiFePO_4$ cells under rapid heating: Rethinking interfacial stability. *J. Power Sources* **2025**, *657*, 238165. DOI:10.1016/j.jpowsour.2025.238165
35. Preger Y, Barkholtz HM, Fresquez A, Campbell DL, Juba BW, Romàn-Kustas J, et al. Degradation of Commercial Lithium-Ion Cells as a Function of Chemistry and Cycling Conditions. *J. Electrochem. Soc.* **2020**, *167*, 120532. DOI:10.1149/1945-7111/abae37
36. Diaz F, Wang Y, Moorthy T, Friedrich B. Degradation Mechanism of Nickel-Cobalt-Aluminum (NCA) Cathode Material from Spent Lithium-Ion Batteries in Microwave-Assisted Pyrolysis. *Metals* **2018**, *8*, 565. DOI:10.3390/met8080565
37. Hölderle T, Baran V, Schökel A, Westphal L, Stelzer RU, Niewa R, et al. Understanding the Temperature–Induced Decomposition of Commercial Nickel–Cobalt–Aluminum Oxide ($LiNi_{0.8}Co_{0.15}Al_{0.05}O_2$) Electrodes. *Batter. Supercaps* **2025**, *8*, e202500421. DOI:10.1002/batt.202500421
38. Hsu M. Thermal Stability of Lithium Ion Battery Electrolyte. NETZSCH Analyzing & Testing. 18 August 2020. Available online: https://analyzing-testing.netzsch.com/en/blog/2020/thermal-stability-of-lithium-ion-battery-electrolyte (accessed on 20 February 2026).
39. Apeagyei AK, Grenfell JRA, Airey GD. Application of Fickian and non-Fickian diffusion models to study moisture diffusion in asphalt mastics. *Mater. Struct.* **2015**, *48*, 1461–1474. DOI:10.1617/s11527-014-0246-2
40. Zhokh A, Strizhak P. Crossover between Fickian and non-Fickian diffusion in a system with hierarchy. *Microporous Mesoporous Mater.* **2019**, *282*, 22–28. DOI:10.1016/j.micromeso.2019.03.016
41. Oladoja NA. A critical review of the applicability of Avrami fractional kinetic equation in adsorption-based water treatment studies. *Desalination Water Treat.* **2016**, *57*, 15813–15825. DOI:10.1080/19443994.2015.1076355